

Hybrid physics-data-driven modeling for sea ice thermodynamics and transfer learning

G. De Cillis¹, A. Carrassi^{1,5}, J. Brajard², L. Bertino², M. Broccoli³, D. Iovino³, T.S. Finn⁴, and M. Bocquet⁴

¹Department of Physics and Astronomy “Augusto Righi”, Bologna, 40126, Italy

²Nansen Environmental and Remote Sensing Center, Jahnebakken 3, Bergen, N-5007, Norway

³CMCC Foundation - Euro-Mediterranean Center on Climate Change, Bologna, Italy

⁴CEREA, ENPC, EDF R&D, Institut Polytechnique de Paris, 6-8 avenue Blaise Pascal, Cité Descartes, Marne-la-Vallée, 77455, France

⁵Department of Meteorology, University of Reading, Reading, UK

February 2, 2026

Abstract

This study explores a physics–data driven hybrid approach for sea-ice column physics models, in which a machine learning (ML) component acts as a state-dependent parameterization of forecast errors. We examine how perturbations in snow thermodynamics and sea-ice radiative properties affect forecast errors, and train dedicated neural networks (NNs) for each model configuration. The performance of the hybrid models is evaluated for long lead-time forecasts and compared against a benchmark system based on climatological forecast-error estimates. The NN-based hybrids prove to be stable, robust to initial condition and atmospheric forcing errors, and consistently outperform their climatology-based counterpart. To derive guiding principles for efficiently handling possible physical model updates, we perform transfer learning experiments to test whether pretrained NNs optimized for one model configuration can be successfully adapted to another. Results indicate that direct evaluation of pretrained networks on the target task provides useful insights into their adaptability, recommending transfer learning whenever performance exceeds a trivial baseline. Finally, a feature-importance analysis shows that atmospheric forcing inputs have negligible influence on NN predictive skill, while ice-layer enthalpies play a key role in achieving satisfactory performance.

Keywords — sea ice, forecast error, hybrid models, neural networks, transfer learning

1 Introduction

Over the past 15 years, machine learning (ML) has experienced exceptional growth, driven by remarkable progress in computational power and the pivotal introduction of GPU-accelerated training for deep neural networks as demonstrated with the breakthrough in image classification by Krizhevsky et al. (2012) with AlexNet. Since then, ML applications have permeated a wide range of scientific and technological domains, among which numerical weather and climate modeling has emerged as a prominent example, enabled by the extension of computer vision techniques to the geosciences.

Recent advancements have enabled the development of global, fully data-driven, ML-based weather prediction (MLWP) systems (Pathak et al., 2022; Lam et al., 2023; Bi et al., 2023; Chen et al., 2025; Bodnar et al., 2025). Trained primarily on ERA5 reanalysis data (Hersbach et al., 2020), these models have shown comparable and sometimes superior skills with respect to ECMWF’s deterministic operational forecasting system, IFS-HRES, on short-to-medium range forecasts (Rasp et al., 2024). The main advantage of these models is their exceptional computational speed and efficiency, compared to classical physics-based models. However, they could remain limited by their lack of physical consistency and realism (Bonavita, 2024), which are crucial for meteorology in complex terrain, extreme event, coupled phenomena, as well as for seasonal and climate predictions. Additionally, the majority of them rely on high resolution physics-based models and data assimilation (DA) for their training and initialization.

Another pragmatic approach, more conservative, is represented by hybrid modeling that combines ML with traditional physics-based models, in an attempt to extract the best of both while mitigating their individual weaknesses.

This combination is often achieved through the replacement of physics-based or empirical parameterizations with data-driven ML components, with the aim of improving accuracy or reducing computational cost (Chevallier et al., 1998; O’Gorman and Dwyer, 2018; Rasp et al., 2018; Bolton and Zanna, 2019). In the context of sea ice modeling, Driscoll et al. (2024) trained Neural Networks (NNs) to emulate an advanced physics-based melt pond parameterization within the ice column model Icepack (Hunke et al., 2025), while Horvat and Roach (2022) focused on wave-induced ice floe fracturing through a neural-network emulation of a computationally expensive super-parameterization.

Despite continuous progress, numerical weather and climate model predictions inevitably remain affected by systematic errors, due to discretization errors, imperfect subgrid-scale parameterizations or inaccurate boundary conditions, initial conditions and forcings. Therefore, instead of focusing on specific process parameterizations, another research branch on hybrid modeling targeted the model error, developing ML-based model error parameterizations that complement physically derived models during execution (Watson, 2019). Similar to MLWP models, these hybrid models for model error correction leverage DA that, along with the increasing volume and quality of observational data, plays a fundamental role in geoscience, by providing optimal estimates (*analyses*) of the state of the earth system (Carrassai et al., 2018). In particular, *analysis increments* (differences between analysis and forecast states) are exploited to infer state-dependent systematic model errors (Carrassai and Vannitsem, 2011). Key contributions along these lines include the work of Brajard et al. (2021) and Farchi et al. (2021b), who trained NNs as additive integrated correction term between two forecast times, i.e. in the *resolvent* of geophysical models, learning from analysis increments, with particular focus on the role of observation noise and sparseness. Farchi et al. (2021a) further investigated the potential of tendency correction and introduced an *online learning* strategy, in which both the model states and the model parameter are estimated at the same time as soon as new observations become available. Similar approaches to hybrid modeling have also been applied to more realistic scenarios, such as the work of Watt-Meyer et al. (2021), who trained a ML model to emulate nudging tendency terms within a weather forecast system; Farchi et al. (2025) who learned a neural network correction to the Integrated Forecasting System of the ECMWF both offline and online; Du et al. (2025), who developed ML-based corrections for ocean mixed-layer temperature biases in a global climate model; and Chapman and Berner (2025), who improved multidecadal atmospheric predictions through online bias correction trained on nudging increments. This type of hybrid modeling has also been explored for sea ice. For example, Finn et al. (2023) employed convolutional U-nets to parametrize model error due to unresolved subgrid scale of sea-ice dynamics within an unstructured finite element model with a Maxwell elasto-brittle rheology. More recently, Gregory et al. (2024) successfully trained Convolutional Neural Networks (CNNs) to correct systematic errors of a global coupled ocean-sea ice model, demonstrating improvements achieved by iterating DA and ML steps (Bocquet et al., 2020). Building on this work, Gregory et al. (2026) developed a hybrid global coupled ice-atmosphere-ocean climate model, highlighting the importance of fully coupled training for generalization in free forecasts. He et al. (2025) applied ML for online error correction within an earth system model for seasonal arctic sea ice prediction and compared it with an offline approach where ML post-processes and calibrates model predictions after the simulation.

In the present study, we build upon previous works to develop state-dependent, ML-based resolvent corrections for the sea-ice column model, Icepack. Model errors are introduced by perturbing parameters related to snow thermodynamics and radiative properties, while synthetic observations are generated using a reference configuration. Neural networks are trained to predict systematic forecast errors, conditioned on the forecast model state. The online execution of the hybrid models, therefore, combines consecutive forecast steps with NN-based corrections, in a similar fashion as sequential DA algorithms. This hybrid framework enables a detailed assessment of how specific parametric model errors influence forecasts and the corresponding ML bias corrections. Insights into the relative importance of predictors for estimating model error, and indications for a shared minimal model, are obtained through recursive feature elimination analyses applied across all perturbed configurations.

An important, yet often overlooked, challenge in the operational deployment of model-error-correcting hybrid systems is the impact of model updates (i.e., when a new model enters into play, with e.g. new parameterizations, numerical schemes, etc.), which can cause abrupt shifts in error statistics. Unlike gradual changes induced by climate variability, which can be addressed with online learning strategies, model version updates require dedicated measures. The most straightforward approach is to generate a reanalysis with the updated model over a sufficiently long period and retrain the ML component. However, this is computationally demanding, and transfer learning strategies offer a promising alternative to reduce the amount of new data required for network adaptation. In this study, we conduct detailed novel transfer learning experiments, focusing on investigating the extent to which an ML model optimized for bias correction in one physical model can then be successfully adapted to another through fine-tuning. The effectiveness of this approach is evaluated as a function of the available new training dataset size and we propose a criterion to determine when fine-tuning is more advantageous than retraining from scratch. This may guide strategic choice on whether and when a new complete retraining may be avoided while keeping the model performance satisfactory.

This article is structured as follows. Section 2 introduces the numerical physics-based model, including reference and perturbed configurations. Section 3 illustrates the hybrid framework, covering training data generation, NNs training, and online execution of hybrid models. Neural networks validation and hybrid models testing are presented in Section 4. Section 5 presents transfer learning experiments, and a feature importance study is provided in Section 6. Finally, summary and conclusions are given in Section 7.

2 The Icepack column physics model

2.1 Model description

Icepack is a submodule of the Los Alamos Sea Ice Model (CICE) (Hunke et al., 2024), designed to simulate all vertical processes within sea ice, such as thermodynamics and mechanical redistribution (ridging), and related changes in ice area and thickness. In addition to the column physics code, the Icepack module includes a driver code, which enables standalone testing of the physics code on individual, independent grid points. The present work is based on pointwise sea ice simulations using the Icepack standalone driver. To represent subgrid-scale thickness variability, Icepack uses the Ice Thickness Distribution (ITD) parameterization (Thorndike et al., 1975), whose transport equation is solved using the remapping method of Lipscomb (2001). In this work, $C = 5$ thickness categories are used, each discretized into seven vertical ice layers and a single snow layer. These categories represent bins of the underlying ITD. For each category, both ice concentration (area fraction) and ice volume are defined, with the set of concentration values providing a discrete approximation of the ITD. The model is driven by atmospheric forcing consisting of downward radiative fluxes, air temperature, relative humidity, total precipitations and wind speed from ERA5 reanalysis data (Hersbach et al., 2020). The coupled ocean is modeled using a mixed-layer model with deep ocean heat flux set to zero and constant salinity. All simulations in this study employ the level-ice melt pond parameterization (Hunke et al., 2013), the mushy layer thermodynamics (Turner et al., 2013), and a 3-band Delta-Eddington radiative transfer scheme.

2.2 Reference and perturbed configurations

We introduce model error by perturbing the reference model configuration. Specifically, we focus on errors arising from the misspecification of two key model parameters: (1) the thermal snow conductivity (`ksno`), which controls the heat flux through the snow layer and thus its insulating effect, and (2) the maximum melting snow grain size (`rsnw_mlt`), a parameter of the delta-Eddington radiation scheme that influences snow albedo estimates. This choice was guided by the findings of Urrego-Blanco et al. (2016), who demonstrated that model predictions are particularly sensitive to these two parameters. Additionally, the authors provided uncertainty estimates for model parameters using statistical distributions, as detailed in Table 1. The reference configuration, used to produce trajectories assumed as true, utilizes the default values of these parameters (cf. Tab. 1). To explore the perturbed

Symbol	Description	Default value	Distribution	Min value	Max value	Mode
<code>ksno</code>	Thermal snow conductivity ($\text{W m}^{-1}\text{K}^{-1}$)	0.3	Uniform	0.03	0.65	
<code>rsnw_mlt</code>	Max. melting snow grain size (μm)	1500	Triangular	250	3000	1500

Table 1: Parameter descriptions and statistical distributions (Urrego-Blanco et al., 2016)

parameters subspace, an ensemble of $M = 30$ independent model configurations is generated by sampling each parameter from its respective distribution. Each model parameter configuration is uniquely identified by its member ID (`m_01`, `m_02`, ..., `m_30`), which is used hereafter. The amplitude of the perturbations and the degree of similarity across configurations are examined in Section S1 of the Supporting Information. Simulations are run in $L = 6$ locations (Figure 1), selected as representative of the diverse sea-ice conditions observed across the Arctic. The reference configuration is firstly run for 30 years, applying cyclically the first year (1993) atmospheric forcings (Figure S1a). This allows us to obtain a stable sea ice annual cycle, which provides initial conditions for the 15-year reference runs (Figure S1b). Prediction errors over long lead times due to parameter perturbations are evaluated by running the 30 perturbed models, initialized with true states, for 15 years. Resulting ice volume forecasts are presented in Figure 2. It can be noted that at higher latitudes (left panels), ice volume errors pile up over years, reaching values up to 2 meters. On the other hand, at lower latitudes (right panels), ice volume errors do not accumulate over years as the sea ice is completely melted every summer. Nonetheless, short-term errors in these regions cannot be neglected, especially in 2D configurations where advection may propagate them to other areas. The effect of climate change driven by atmospheric forcing is also evident in Figures 2a and 2c, which show

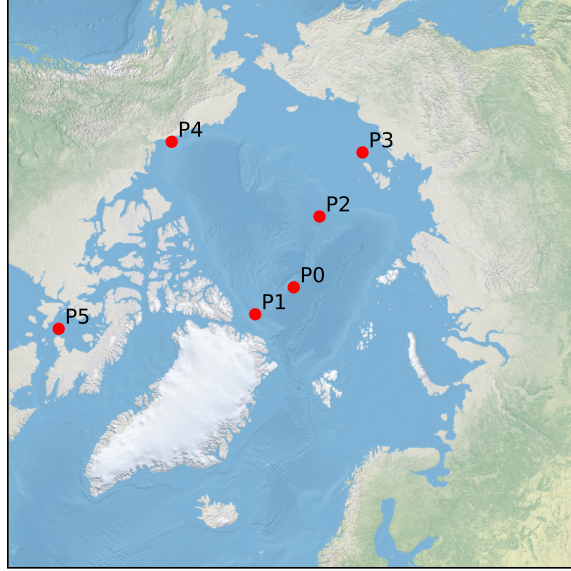


Figure 1: Locations of Icepack simulations, selected from the ERA5 grid downsampled to 1°resolution, at latitudes between 65°N and 90°N.

a gradual decline in ice volume over the years. As we shall see, this non-stationarity challenges the extrapolation capabilities of the ML algorithm for forecast error correction.

3 Hybrid framework

The hybrid model developed in this work combines the physics-based Icepack model with an additive ML component that acts as a correction to the model resolvent. Trained on DA analysis increments, the ML component estimates systematic forecast biases at a prescribed lead time and iteratively corrects the model state. The rationale for this approach is that when the analyses are accurate enough to serve as proxies for the unknown true states (e.g., negligible analysis error), the corresponding analysis increments largely reflect forecast errors arising from model deficiencies (Carrassi and Vannitsem, 2011). Under these assumptions, analysis increments provide suitable training targets for ML models that estimate state-dependent model error conditioned on forecast states (Bocquet et al., 2020; Brajard et al., 2021; Farchi et al., 2021a; Bocquet, 2023; Finn et al., 2023). The resulting hybrid approach is, therefore, reminiscent of a sequential DA cycle, with the ML corrections in place of analysis increments, as detailed in Section 3.3.

In this study, training data are generated in an idealized setting with perfect, complete observations: under this assumption, the effect of initial condition error is eliminated. This intentional simplification allows us to focus on ML design and performance and to study in detail the strength and limitation of the proposed approach without the confounding effect derived from the presence of initial condition error and its interplay with the model error. The latter issue is addressed in the online hybrid model experiments (Section 4.3).

3.1 Training data generation

Given the assumption of perfect complete observations, for each location and model configuration, incorrect forecast trajectories \mathbf{x} are produced by initializing models from "true" reference full states \mathbf{x}^t at $S^{\text{tr}} = 522$ dates, $\{t_s\}$, spanning the period from 1 January 1994 to 31 December 2003, with a weekly stride $\tau_w = 7$ days:

$$\mathbf{x}_{t_s+\tau} = \mathcal{M}_{t_s:t_s+\tau} (\mathbf{x}_{t_s}^t, \mathbf{F}_{t_s:t_s+\tau}), \quad (1a)$$

$$t_s = t_0 + (s-1)\tau_w, \quad s = 1, \dots, S^{\text{tr}} \quad (1b)$$

where $\mathcal{M}_{t_s:t_s+\tau}$ denotes the resolvent of the physics-based model from time t_s to $t_s + \tau$, and $\mathbf{F}_{t_s:t_s+\tau}$ the corresponding atmospheric forcings over the forecast window. Each simulation is run up to a maximum lead time $\tau = 180$ days, with outputs stored every 5 days.

The analysis of forecast error statistics as a function of lead time and initialization date (Section S2, Supporting Information) led to selecting a fixed training lead time of $\tau_{\text{tr}} = 60$ days, which provides a suitable balance between

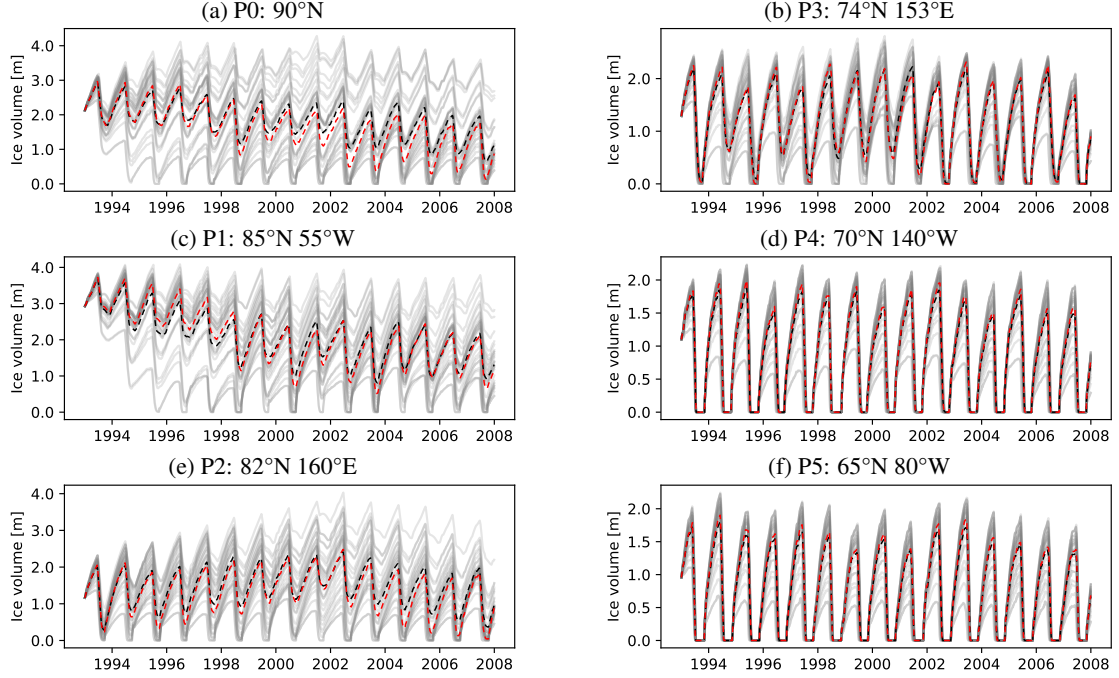


Figure 2: Ice volume time-series over a 15-year period at the 6 selected locations: red dashed lines (---) indicate the truth; solid grey lines (—) show forecasts from individual models with perturbed parameters; black dashed lines (----) denote the forecast ensemble means.

forecast degradation and signal strength. In more realistic settings, the forecast is expected to degrade faster, leading to a shorter training lead time. In general, a suitable balance should exist for any reasonable forecast model. Machine learning datasets are then constructed by pairing features with targets at the selected lead time τ_{tr} . The targets are the forecast errors, $e_s = \mathbf{x}_{t_s+\tau_{\text{tr}}} - \mathbf{x}_{t_s+\tau_{\text{tr}}}^t$, while the feature vectors, $\mathbf{z}_s = \mathcal{G}(\mathbf{x}_{t_s+\tau_{\text{tr}}}, \mathbf{F}_{t_s+\tau_{\text{tr}}})$, comprises model state variables, atmospheric forcings and diagnostics at time $t_s + \tau_{\text{tr}}$, where \mathcal{G} selects and/or derives the predictors used as ML inputs. The resulting supervised learning dataset, combining data from all locations, for a single perturbed configuration is $\mathcal{D} = \{(\mathbf{z}_i, e_i)\}_{i=1}^N$, and counts $N = L \times S^{\text{tr}} = 3132$ instances.

3.2 Machine learning regression task

The objective of the ML model is to approximate the mapping between input features \mathbf{z} and the forecast error \mathbf{e} through a NN, $\mathbf{g}(\theta, \mathbf{z})$, where θ denotes the network trainable parameters. In this study, we focus on predicting the component-wise forecast errors in ice concentration, $\mathbf{a} = (a_1, \dots, a_C)$, and ice volume, $\mathbf{v} = (v_1, \dots, v_C)$. Two independent NNs, for ice concentration and ice volume, are implemented to prevent cross-task interference and ensure stable learning. Each network is trained by minimizing the following cost function,

$$\mathcal{L}(\theta^\varphi) = \overline{(\mathbf{g}(\theta^\varphi, \mathbf{z}_i) - \mathbf{e}_i^\varphi)^2}, \quad \varphi \in \{\mathbf{a}, \mathbf{v}\} \quad (2)$$

where $\overline{(\cdot)}$ denotes the average over the dataset instances and the five ice categories, and \mathbf{e}_i^φ represents the forecast error, with φ indicating either ice concentration or ice volume. The NN functional form \mathbf{g} (i.e., its architecture) is identical for both ice concentration and volume; the distinction arises solely from the respective trained weights. The inputs and targets are normalized by per-variable means and standard deviations, estimated from the training dataset. Table 2 summarizes the target and features variables used.

At inference time, the combined NN error prediction is given by

$$\mathbf{g}(\hat{\theta}, \mathbf{z}) = [\mathbf{g}(\hat{\theta}^a, \mathbf{z}), \mathbf{g}(\hat{\theta}^v, \mathbf{z})] \quad (3)$$

where $\mathbf{g}(\hat{\theta}^a, \mathbf{z})$ and $\mathbf{g}(\hat{\theta}^v, \mathbf{z})$ denote the trained networks' predictions for ice concentration and ice volume, respectively.

	Symbol	Description	Dimension
Features	ftrain	Precipitation	1
	fswabs	Absorbed short wave	1
	flw	Longwave radiation	1
	flwout	Outgoing longwave	1
	fsnow	Snowfall	1
	Tair	2m air temperature	1
	aicen	Ice concentrations	5
	vicen	Ice volumes	5
	vsnon	Snow volumes	5
	Tsfcn	Ice surface temperature	5
	qice001	Ice enthalpy - layer 1	5
	qice002	Ice enthalpy - layer 2	5
	qice003	Ice enthalpy - layer 3	5
	qice004	Ice enthalpy - layer 4	5
	qice005	Ice enthalpy - layer 5	5
	qice006	Ice enthalpy - layer 6	5
	qice007	Ice enthalpy - layer 7	5
Targets	err_a (err_v)	Ice concentration (volume) errors	5

Table 2: Features and targets of NN model. Variables with dimension 5 are defined over the ITD categories used by default in Icepack.

Neural network architecture As a column model, Icepack is horizontally pointwise, involving only the vertical and categorical dimensions in addition to time. Based on this structure, Multilayer Perceptrons (MLPs) are trained, using LeakyReLU activation functions in the hidden layers and linear activations in the output layer. Depth and width of the hidden layers, as well as the learning rate and batch size are selected through hyperparameter optimization using Asynchronous Successive Halving (ASHA) (Li et al., 2020). The search space includes MLP architectures having from one to three hidden layers, with hidden-layer widths between 10 and 60 neurons, learning rates sampled on a logarithmic scale in the range 10^{-4} to 10^{-1} , and batch sizes drawn from a small set of standard values. The resulting configuration consists of two hidden layers with 20 neurons each, trained using Adam optimization (Kingma and Ba, 2017), with learning rate $\gamma = 8 \times 10^{-4}$, weight decay $\lambda = 10^{-4}$ and batch size $N_b = 32$.

3.3 Icepack–NN hybrid model

The hybrid model we develop is designed to iteratively correct forecast errors during model execution. Among all the Icepack state variables, we predict and correct errors for the most relevant: the ice concentration and the ice volume for the five ice thickness categories. Figure 3 illustrates a single hybrid model iteration. It consists of a forecast step,

$$\mathbf{x}_{t_{k+1}} = \mathcal{M}_{t_k:t_{k+1}} \left(\mathbf{x}_{t_k}^{\text{hyb}}, \mathbf{F}_{t_k:t_{k+1}} \right), \quad (4a)$$

$$t_{k+1} - t_k = \tau_{\text{tr}}, \quad (4b)$$

where, starting from initial conditions $\mathbf{x}_{t_k}^{\text{hyb}}$, the model is integrated forward under atmospheric forcings $\mathbf{F}_{t_k:t_{k+1}}$, to produce the uncorrected forecast state $\mathbf{x}_{t_{k+1}}$. The second step involves the forecast error correction:

$$\tilde{\mathbf{x}}_{t_{k+1}}^{\text{hyb}} = \mathbf{x}_{t_{k+1}} - \mathbf{g}(\hat{\theta}, \mathbf{z}_{t_{k+1}}), \quad (5)$$

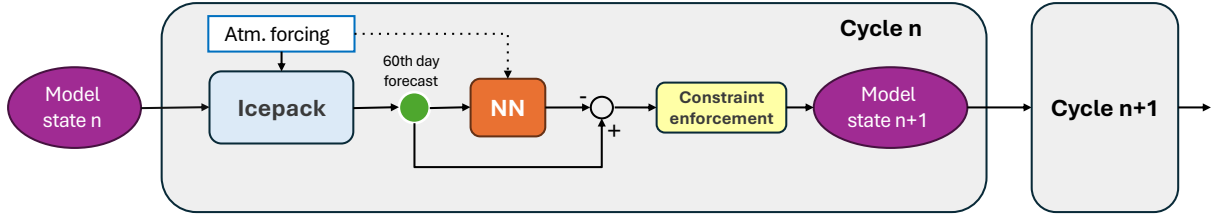


Figure 3: Schematic of the hybrid model loop.

where NN error predictions $g(\hat{\theta}, z_{t_{k+1}})$ are subtracted from the forecast state. This produces an intermediate hybrid model state $\tilde{x}_{t_{k+1}}^{\text{hyb}}$, that is adjusted in a final step:

$$x_{t_{k+1}}^{\text{hyb}} = \Pi^{\text{con}}(\tilde{x}_{t_{k+1}}^{\text{hyb}}), \quad (6)$$

where a post-processing, Π^{con} , is applied to obtain the final hybrid model state $x_{t_{k+1}}^{\text{hyb}}$. The post-processing step, corresponding to the box *Constraint enforcement* in Figure 3, is necessary to enforce specific constraints, such as non-negativity of ice concentration and volume, as well as the requirement that ice concentrations must not exceed one. All adjustments introduced to ensure physical and model consistency are detailed in paragraph below, *Treatment of bounded variables*. The model state obtained after post processing represents the initial condition for the subsequent iteration.

Treatment of bounded variables Ice volumes and concentrations, their total values as well as those associated with each thickness category, are bounded quantities: $v_c \in [0, +\infty)$, $a_c \in [0, 1]$, $\sum_c a_c \in [0, 1]$. Recall that $c = 1, \dots, 5$ indicates the ice category. When applying ML-based corrections, these bounds are not guaranteed to be respected. Violations typically occur when both the forecast concentration or volume and the true error are close to zero; in these cases, minor inaccuracies in the NN correction can produce slightly negative values. Although these violations are generally of negligible magnitude, it is essential for the hybrid model that all prognostic variables remain within their physical bounds to ensure successful numerical integration. The motivation for enforcing bounds differs here from what motivates their implementation in, e.g. ML surrogates for the sea ice (Finn et al., 2024; Durand et al., 2025), whereby the autoregressive use of the NNs obliges their adoption for stabilizing the time evolution. In our case, NN inputs are always provided by the physical model, so the possible instability of the NN is not a primary concern. Instead, our objective is to guarantee physical model consistency and suitable initial conditions for the restart: without proper enforcement of bounds, Icepack may fail to restart or diverge rapidly. Physical consistency (ensuring agreement between volume and concentration, their simultaneous vanishing, and adherence to thickness bounds) can be achieved either by enforcing constraints during training or by applying corrections after the NN outputs. While the latter approach may introduce systematic biases, the former would require a bivariate NN and constrained optimization strategies, adding substantial complexity for limited benefit. For these reasons, and since constrained optimization is not the focus here, constraints are enforced as a post-processing step on the corrected states. The procedure is detailed in the pseudo-code format in Algorithm 1, where h_c^{\min} and h_c^{\max} denote the prescribed minimum and maximum ice thickness for category c , while a tolerance of $\epsilon = 10^{-2}$ m is introduced to prevent assigning thickness values exactly at the bounds. Note that the enforcement of thickness bounds preserves the validity of the total concentration constraint. Finally, additional consistency adjustments are applied to related state variables. Specifically, snow volume and enthalpy are set to zero whenever ice is entirely removed from a given category, while in previously ice-free categories that gain ice, the salinity and enthalpy of the new ice layers are initialized using Icepack's default values.

4 Neural Network and Hybrid Model Evaluation

The development of the NN-based hybrid Icepack models, hereafter referred to as Icepack-NN, involves an initial analysis of the data, followed by NNs training, offline testing, and ultimately, hybrid model validation and performance assessment. Performance is evaluated relative to both the uncorrected Icepack model and a benchmark hybrid configuration, termed Icepack-wclim, which replaces NN predictions with location-independent weekly climatological corrections. Separate NN-based and climatological correction schemes are trained for each Icepack model configuration. The error climatologies are derived from the same training data as the NNs and averaged across locations, ensuring a fair comparison to the location-independent NN predictions. Note that the term *weekly*

Algorithm 1 Post-processing of category variables a_c and v_c

```

1: for  $c = 1, \dots, C$  do                                 $\triangleright$  Enforce non-negativity and ensure consistency between  $a$  and  $v$ 
2:    $a_c \leftarrow \max(0, a_c)$ 
3:    $v_c \leftarrow \max(0, v_c)$ 
4:    $a_c \leftarrow a_c \cdot \mathbf{1}_{\{v_c > 0\}}$ 
5:    $v_c \leftarrow v_c \cdot \mathbf{1}_{\{a_c > 0\}}$ 
6: end for
7:
8: if  $\sum_c a_c > 1$  then                                 $\triangleright$  Renormalize concentrations
9:    $a \leftarrow a / \sum_c a_c$ 
10: end if
11:
12: for  $c = 1, \dots, C$  do                                 $\triangleright$  Enforce ice thickness bounds
13:    $h_c \leftarrow v_c / a_c$ 
14:   if  $h_c \geq h_c^{\max}$  then
15:      $v_c \leftarrow a_c \cdot (h_c^{\max} - \epsilon)$ 
16:   else if  $h_c < h_c^{\min}$  then
17:      $a_c \leftarrow v_c / (h_c^{\min} + \epsilon)$ 
18:   end if
19: end for

```

refers to the averaging time window; the averaged data are still forecast errors at a lead time of 60 days. For the preliminary data analysis and performance evaluation purposes, we consider the root mean square error RMSE^m and bias BIAS^m for each model configuration m , as well as the model ensemble RMSE , RMSE^{ens} , all computed as function of lead time τ :

$$\text{RMSE}^m(\tau) = \sqrt{\frac{1}{N} \sum_{c,l,s} \left(\varphi_c^{m(s,l)}(\tau) - \varphi_c^{\text{t}(l)}(t_s + \tau) \right)^2}, \quad (7)$$

$$\text{BIAS}^m(\tau) = \frac{1}{N} \sum_{c,l,s} \left(\varphi_c^{m(s,l)}(\tau) - \varphi_c^{\text{t}(l)}(t_s + \tau) \right), \quad (8)$$

$$\text{RMSE}^{\text{ens}}(\tau) = \sqrt{\frac{1}{M} \sum_m \text{RMSE}^m(\tau)^2}, \quad (9)$$

where $\varphi_c^{m(s,l)}(\tau)$ represents the forecast ice volume or concentration, relative to model configuration m , ice category c , location l and initialized at start date t_s ; $\varphi_c^{\text{t}(l)}(t_s + \tau)$ denotes the corresponding true value. Summation indices c , l , and s span the C ice categories, L locations, and S simulations (each initialized at a different start date), yielding N instances, whereas in Eq. (9) the index m ranges over the M model configurations. In addition, RMSE metrics are evaluated under alternative averaging strategies by restricting the dataset to specific subsets (e.g., forecast month, start month, or geographical locations). To quantify the RMSE reduction achieved by the corrected Icepack models (Icepack-NN or Icepack-wclim), across the model configurations, relative to the uncorrected baseline, the ensemble-averaged normalized RMSE, $\langle \text{nRMSE} \rangle$, is considered,

$$\langle \text{nRMSE} \rangle = \frac{\sum_m \text{RMSE}^{\text{u},m} \cdot \text{RMSE}^{\text{hyb},m}}{\sum_m [\text{RMSE}^{\text{u},m}]^2} = \sum_m w^m \cdot \text{nRMSE}^m, \quad (10a)$$

$$w^m = \frac{[\text{RMSE}^{\text{u},m}]^2}{\sum_m [\text{RMSE}^{\text{u},m}]^2}, \quad (10b)$$

$$\text{nRMSE}^m = \frac{\text{RMSE}^{\text{hyb},m}}{\text{RMSE}^{\text{u},m}}, \quad (10c)$$

where the superscripts u and hyb denote, respectively, the uncorrected Icepack and a corrected Icepack model (either Icepack-NN or Icepack-wclim). For readability, the explicit dependence on the lead time τ has been omitted.

4.1 Preliminary data analysis

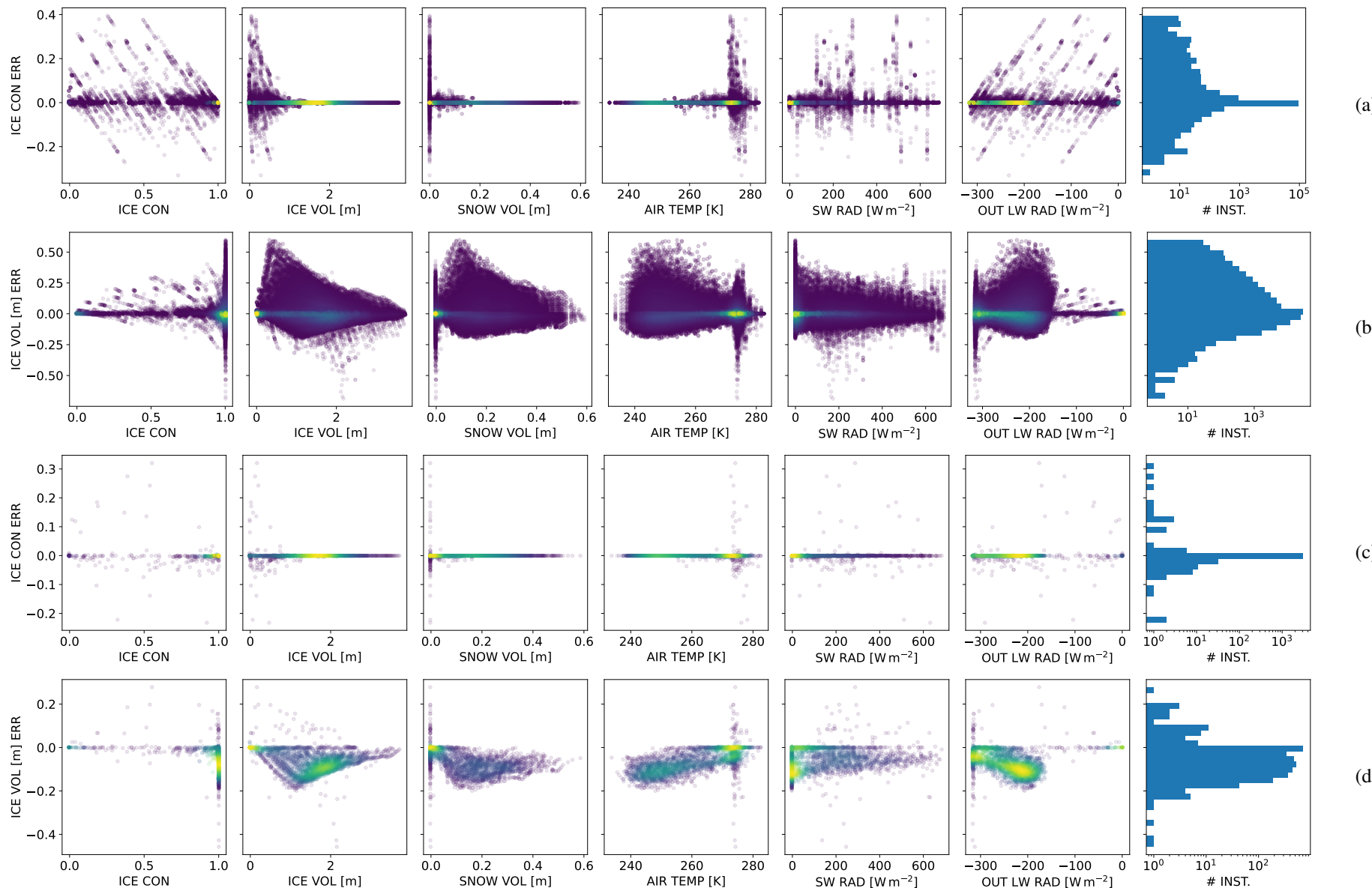


Figure 4: Scatter plots of total ice concentration and volume errors at lead time $\tau = 60$ days, as functions of selected forecast state variables and atmospheric forcings. Point colors represent density estimated via Gaussian KDE. Rows (a) and (b) show data aggregated across all model configurations, whereas panels (c) and (d) show results from model m_05 only.

Figure 4 displays marginal scatter plots extracted from the underlying multivariate distributions relating targets and features, aimed at illustrating the nature of their relationships (e.g. linear, nonlinear, and of which sort). In particular, it shows scatter plots of the errors in ice concentration (rows a and c) and ice volume (rows b and d), cumulated over ice categories, against a selection of forecast model variables and atmospheric forcings. In rows (a) and (b), all data are put together, combining locations, model configurations, and start dates, whereas rows (c) and (d) show the data from a single, arbitrarily chosen, yet representative, configuration (m_05). When data from all perturbed models are aggregated, features and targets appear largely uncorrelated, suggesting that training a neural network to correct forecast errors irrespective of the specific model configuration is not feasible. In contrast, when data associated to a single model configuration are selected, nonlinear relationships between features and ice volume errors become apparent (cf. Figure 4d), indicating that configuration-specific training is more appropriate and consistent with the practical setting in which training data are typically available for a single forecast model. This behavior is not observed for total ice concentration errors (Figure 4c), which are zero in most instances. This apparent lack of variability in total concentration errors stems from the bounded nature of ice concentration: during winters, when the true total concentration reaches 1, the forecast typically does so too, either earlier or later, causing the aggregate error across categories to approach zero. Consequently, these plots may give a misleading impression that concentration errors contain little useful information. In practice, however, our NN is trained on category-wise concentration errors, which evolve over time, even when the total concentration is saturated. Hence, the issue seen in the aggregated plots is expected to be far less pronounced in the actual learning setup.

To characterize the average behavior of each model configuration, we compute the RMSE and BIAS of ice volume and concentration errors from the respective datasets (Figure 5). An approximately linear relationship can be observed between ice volume RMSE and BIAS amplitude (Figure 5a), with the proportion of positively and negatively biased model configurations being nearly equal. On the other hand, ice concentration errors present a markedly different behavior (Figure 5b): biases are extremely small — around three orders of magnitude lower than the RMSEs — with no clear relationship between RMSE and BIAS, and the majority of configurations exhibit negative biases. As noted above, the aggregated ice concentration error is zero in most instances, even if the underlying ITD is inaccurate, so the overall bias remains relatively small.

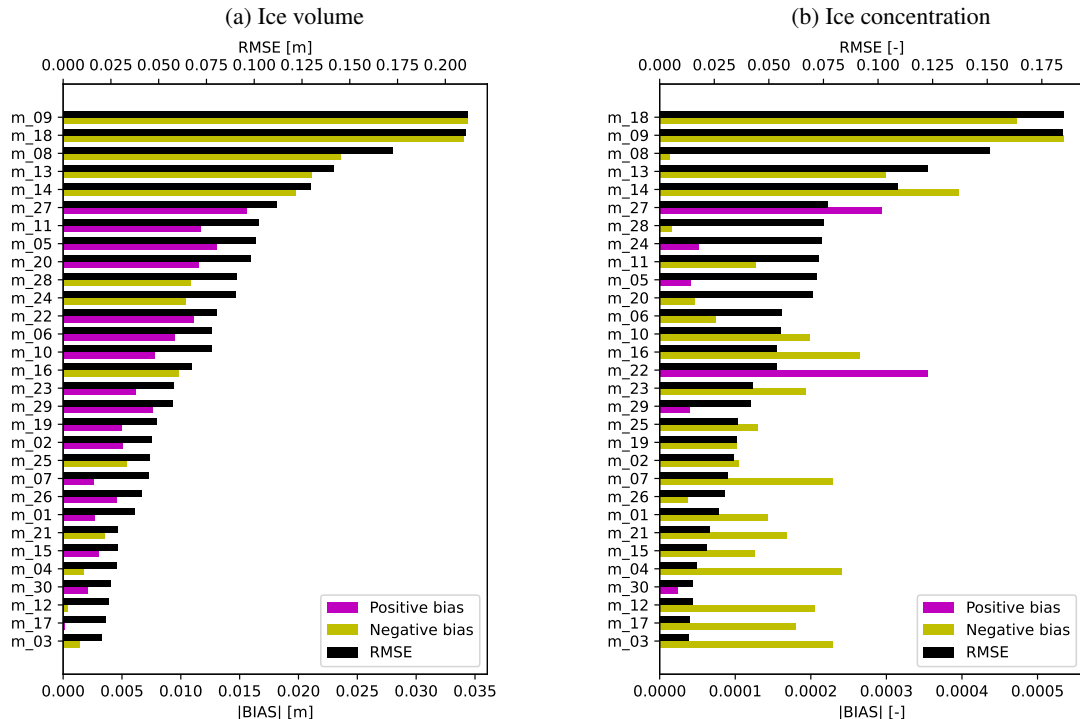


Figure 5: Ice volume (a) and concentration (b) RMSE and BIAS at a lead time of 60 days for all model configurations sorted by the RMSE.

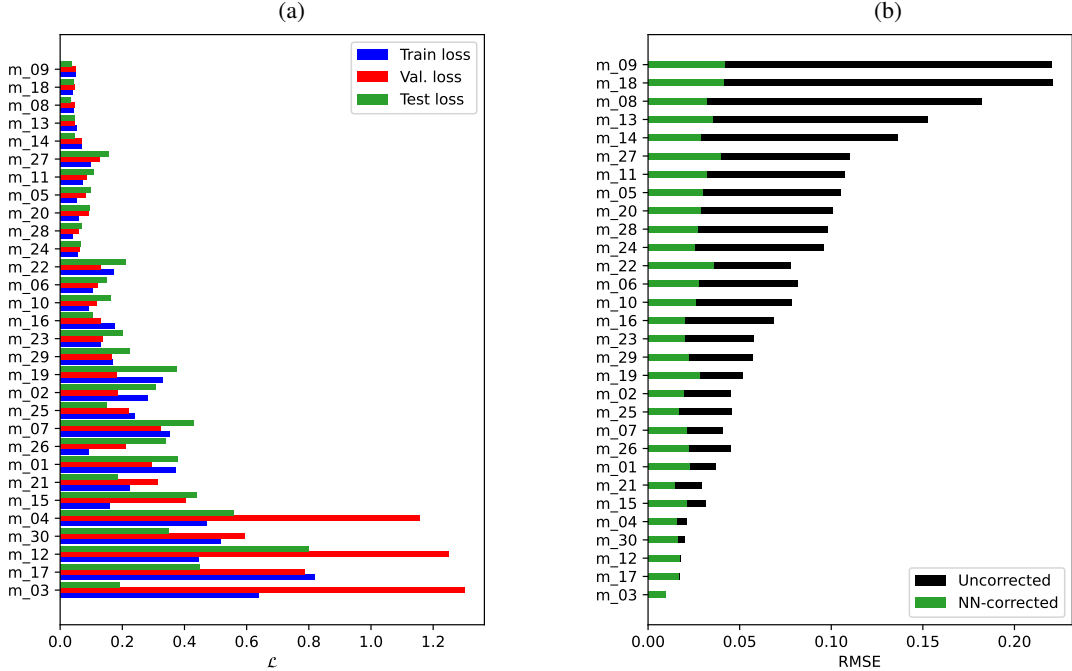


Figure 6: (a) Loss function \mathcal{L} relative to ice volume error prediction, computed over training, validation and test datasets using the best-performing NN for each model configuration. (b) Ice volume RMSE of uncorrected forecasts and its residual value after correction by the NN computed on the test dataset. Model configurations are sorted as in Figure 5(a).

4.2 Neural networks training and offline performance

Motivated by the exploratory analysis in the previous section, separate NNs are trained for each perturbed model configuration using an 8-year dataset spanning 1994 to 2001, totaling 2508 instances. Data from 2002 (312 instances) serve as the validation set, while those from 2003 (312 instances) are held out for testing. The maximum number of training epochs is set to 2000 and validation loss is monitored to apply early stopping and prevent overfitting. Figure 6 and S5 show the results of NNs training performed separately on each dataset corresponding to a given model configuration, for ice volume (Figure 6) and ice concentration (Figure S5) respectively. The values of the loss function \mathcal{L} , computed on training, validation and test datasets using the best-performing NNs (i.e., those achieving the lowest validation loss during training), indicate that the networks perform well for configurations with large forecast errors: where there is room for improvements. When the magnitude of the target forecast errors decreases, their performance deteriorates, even showing overfitting in a few cases. This trend is evident in the right panels of Figures 6 and S5, where both the uncorrected baseline forecast RMSE and the residual RMSE after NN-correction are shown. As forecast RMSE decreases, the relative improvement from NN correction diminishes, and in some cases, the correction even worsens the prediction.

A further quantification of RMSE reduction through the NN correction is presented in Figures 7a and S4a, which show that both the NNs are able to reduce the ice volume and concentration RMSEs by over 80% when the RMSE of the uncorrected models is large. In contrast, for near-perfect models with minimal forecast errors, the NN corrections have a negligible impact. Additionally, Figure 7b shows that, for ice volume, the NN eliminates the bias almost completely and the RMSE is reduced irrespective of the initial bias sign. For ice concentration (Figure S4b), the figure only displays a reduction in RMSE, as the uncorrected forecast bias is already minimal, consistent with the earlier commentary on Figure 5b.

4.3 Hybrid model online testing

4.3.1 Test protocol

Hybrid Icepack-NN models are tested over a four-year period following the data used for training, validation, and offline testing. The primary objective is to evaluate the performance of the hybrid models on long lead time forecasts, assessing, concurrently, their numerical stability, physical consistency and the capabilities to correct forecast error originated by the simultaneous presence of initial condition, atmospheric forcings and model error. Initial

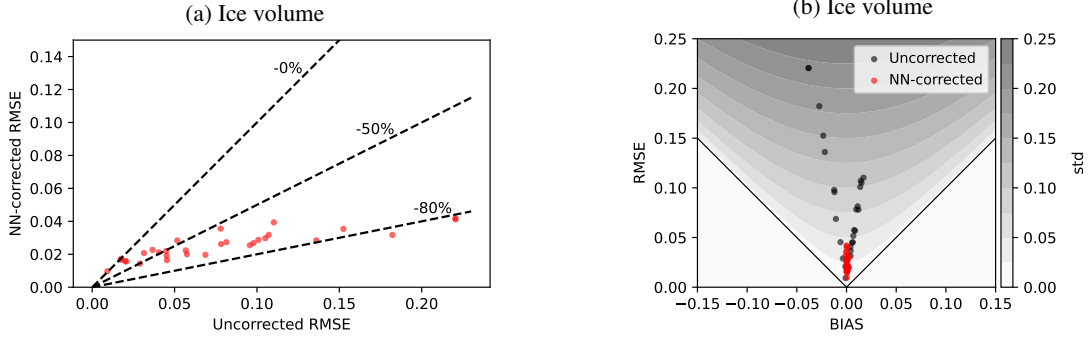


Figure 7: Left panels (a) shows scatter plot of the residual RMSE after NN correction versus the uncorrected Icepack RMSE for ice volume on the test dataset. Dashed lines indicate three levels of RMSE reduction, as labeled in the figure. Right panel (b) displays scatter plots of BIAS and RMSE before and after correction for ice volume, with shaded contours representing the corresponding standard deviation.

condition errors, absent during training, emerge after the first hybrid iteration because NN predictions have inherent errors and only two state variables are updated. Atmospheric-forcing perturbations are introduced to mimic realistic forecasting conditions, in which the forcings provided to the operational hybrid system intrinsically differ from those used during training. This may occur when NNs are trained on analysis increments from reanalyses: the atmospheric forcings used in training come from the reanalysis, whereas during forecasting, the hybrid model is driven by forcing forecasts, which inevitably contain additional errors.

For each of the six locations, we produce 52 forecasts, initialized weekly throughout the year 2004. Each forecast spans 1080 days, corresponding to 18 hybrid model cycles. Hybrid Icepack–NN forecasts are evaluated against both the uncorrected Icepack model and the benchmark Icepack–wclim configuration. Time-correlated perturbations are applied to wind speed and air temperature from ERA5, using a decorrelation time scale of 2 days and standard deviations of 3K and $\sqrt{3}$ m/s, respectively (Sakov et al., 2012; Cheng et al., 2020). These perturbations are identical across all locations and forecasting systems (Icepack, Icepack–NN, and Icepack–wclim), but differ across the 52 start dates. Metrics defined in Equations (7)–(10) are, then, computed over datasets comprising $C = 5$ ice categories, $L = 6$ locations and $S = 52$ simulations with distinct start date, resulting in a total of $N = C \times L \times S = 1560$ data points, for each of the $M = 30$ model configurations.

4.3.2 Performance evaluation

Figure 8 presents ice volume RMSE and BIAS for all model configurations at lead times of 60, 360 and 1080 days, corresponding to 1, 6, and 18 hybrid loops, while Figure 9 highlights the corresponding RMSE reduction achieved by the two hybrid systems. At 60 days, after the first correction, Icepack–NN models display RMSE and BIAS values consistent with those seen in offline evaluations (Figures 7a, 7b), and effectively reduce the forecast errors of the uncorrected Icepack model. In contrast, at the same lead time, Icepack–wclim models, although effective in reducing BIAS, show limited ability to reduce RMSE, as evident in the first panel of Figure 9, where the blue dots are almost aligned with the -0% reference line. At longer lead times, error magnitudes increase for all model configurations. Yet the Icepack–NN models continue to outperform the Icepack–wclim models, with the performance gap between the two hybrid approaches being more pronounced for configurations with positive BIAS (i.e. those that overestimate ice volume), which are generally associated with high snow conductivity (low insulation). In these cases, the Icepack–wclim models perform noticeably worse, as shown by the blue cross markers in the 360- and 1080-day panels of Figure 9, which indicate a systematically smaller RMSE reduction. Such behaviour is reflected in the corresponding panels of Figure 8, where the blue dots display an asymmetric distribution, with larger RMSE values predominantly associated with positive BIAS on the right side of the plot. While our analyses do not provide a definitive explanation, we conjecture that this performance gap is likely associated with an increased sensitivity to initial conditions at the beginning of the melting season, which leads to degraded Icepack–wclim predictions. In contrast, the Icepack–NN models retain high skill, indicating a greater ability to cope with the resulting internal variability.

To provide an ensemble-level perspective on forecast errors and their reduction by the hybrid systems, Figure 10 shows the time series of the RMSE^{ens} for the uncorrected Icepack models (top panel) and the $\langle \text{nRMSE} \rangle$ (bottom panel) for the Icepack–NN and Icepack–wclim models. For both ice concentration and ice volume, the RMSE^{ens} of the uncorrected models increases rapidly during the first 200 days before stabilizing, approaching an almost stationary value after about one year as the models drift toward their own stable annual sea-ice cycles. In the

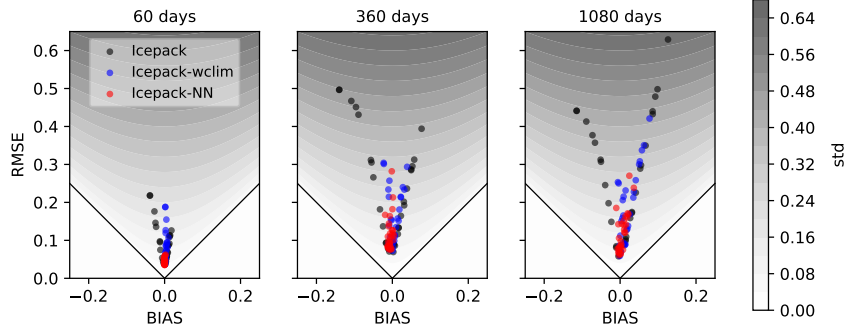


Figure 8: Scatter plots showing ice volume BIAS and RMSE for the uncorrected Icepack models (black dots), and the corrected hybrid models Icepack-NN (red dots) and Icepack-wclim (blue dots), at three different lead times (60, 360, 1080 days).

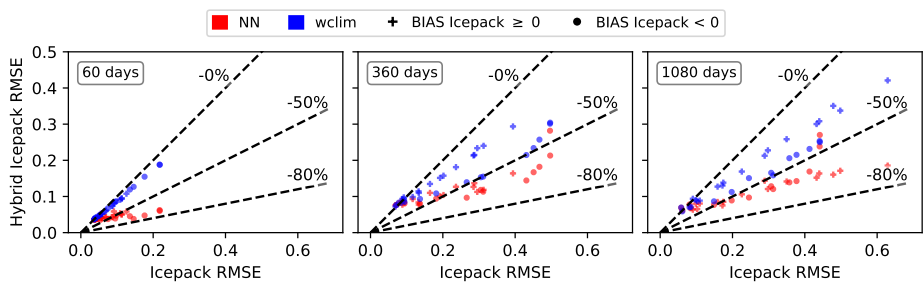


Figure 9: Scatter plots showing the ice volume RMSE for the hybrid Icepack models against the uncorrected Icepack RMSE at three different lead times (60, 360, 1080 days). Crosses/circles mark positive/negative BIAS in the uncorrected Icepack models. The dashed lines mark three percentages of RMSE reduction, which are indicated on the figure.

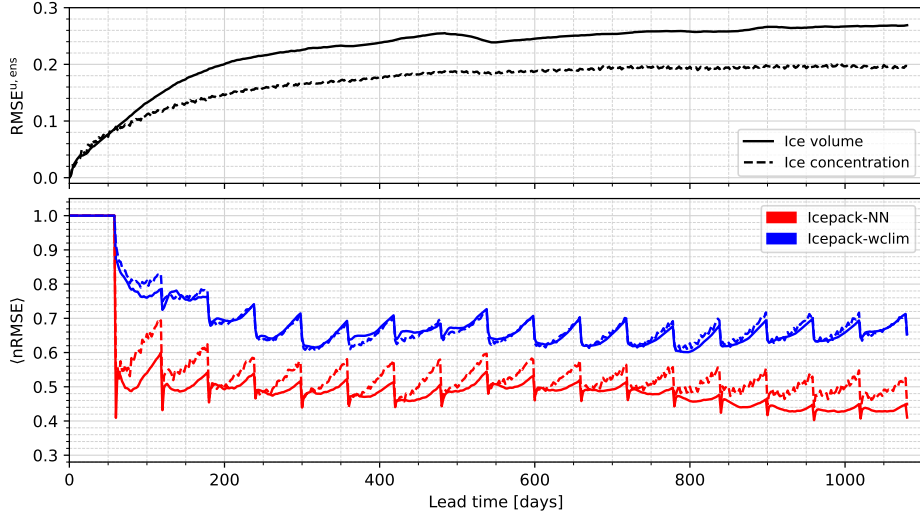


Figure 10: The top panel shows $\text{RMSE}^{\text{u},\text{ens}}$ for the uncorrected Icepack ensemble (Eq. 9) as a function of lead time. The bottom panel displays corresponding $\langle \text{nRMSE} \rangle$ for the Icepack-NN and Icepack-wclim forecasts (Eq. 10). In both panels, solid and dashed lines denote the ice-volume and ice-concentration metrics, respectively.

bottom panel, the $\langle \text{nRMSE} \rangle$ values — corresponding to the slope of a least-squares regression line fitted to the scatter plot data of Figure 9 — highlight the discrete-time nature of the hybrid systems, characterized by periods of error growth between successive impulsive corrections. The superior performance of the Icepack-NN models is evident, with $\langle \text{nRMSE} \rangle$ for ice volume reaching values close to 0.4 at long lead times, whereas the corresponding Icepack-wclim value stays above 0.6. Moreover, although the error reduction provided by Icepack-wclim remains relatively stable, a slight upward trend in its $\langle \text{nRMSE} \rangle$ values is visible. In contrast, the Icepack-NN curves show a slow decline after approximately 600 days, indicating a gradual improvement over long lead times. The performance assessment is completed by examining how the ice-volume RMSE varies with geographic location. Figure 11 displays the seasonal evolution of RMSE at a fixed lead time of 1080 days. For the uncorrected Icepack model, all locations exhibit a pronounced annual cycle, with generally lower RMSE values from July to November and higher values from December to June. A similar seasonal pattern is also visible in the hybrid systems, although it is less pronounced, particularly at the higher-latitude sites P0, P1, and P2. Overall, while both hybrid approaches reduce errors relative to the uncorrected forecast, the Icepack-NN configuration delivers the best performance. At the lower-latitude locations P3, P4, and P5, the errors to be corrected are smaller, and the performance of the two hybrid systems becomes more similar. This is partly because the MSE loss used during training directs the NN to prioritise larger target values. In these locations, during the late-summer to early-autumn period, when the true ice volume is zero, Icepack-NN is systematically worse than both the uncorrected model and Icepack-wclim, although the resulting error remains very small. Here, the uncorrected forecasts are already highly accurate, and the climatological correction does not introduce additional error, whereas the NN retains a small amount of residual variability despite the true target being zero.

5 Adapting to physical model updates: transfer learning

5.1 Motivation

We have so far worked under the common assumption that the process underlying our dataset is autonomous (i.e. it does not explicitly depend on time) or stationary. Under this condition, offline training is, in principle, effective and its accuracy typically improves asymptotically as the size of the training dataset increases. The stationary/autonomous assumption does not hold in many realistic scenarios: notably, it does not so in climatic data in the presence of climate change. A number of solutions have been explored in the literature, in the context of model error correction. When the process statistics do not change too quickly, online learning (Farchi et al., 2021a) and running training strategies (He et al., 2025) have shown promising results. Here we envisage a qualitatively different scenario: the model or the DA system on which the training has been performed undergoes an update (e.g. new parameter calibration), producing a sudden shift in the process statistics. In such cases, while avoiding a new offline training may be desirable, for computational or general feasibility issues, methods designed for

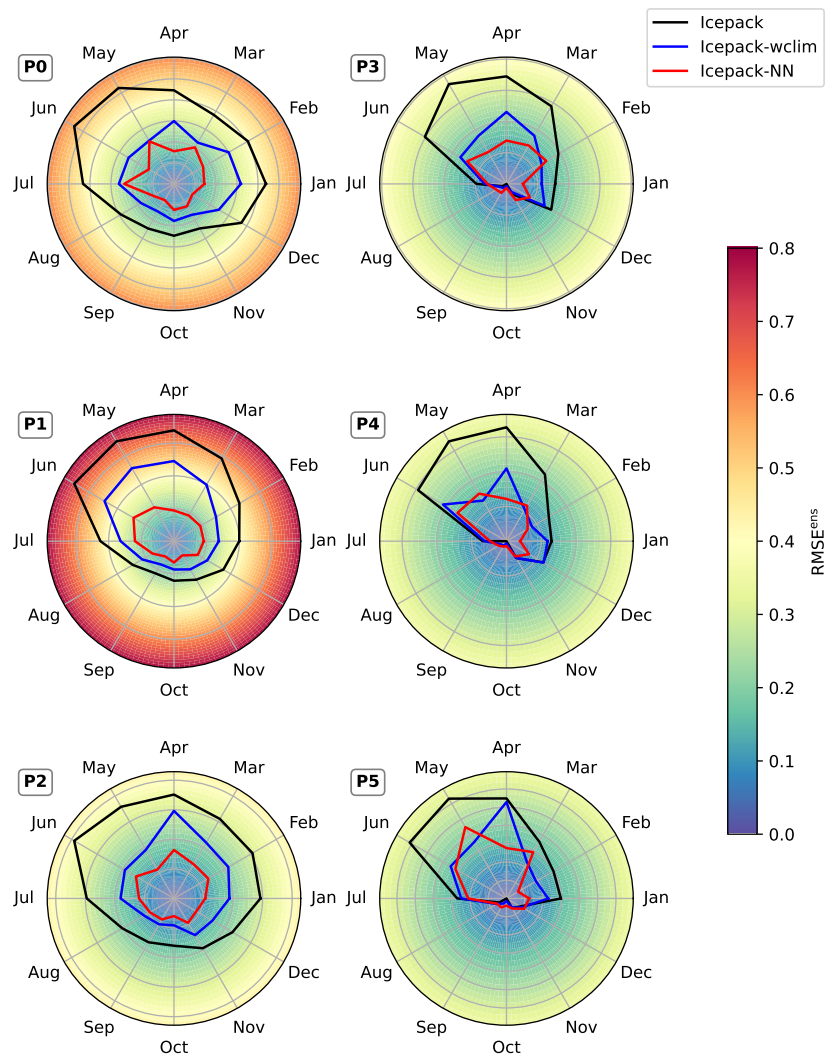


Figure 11: Ice volume RMSE^{ens} as function of forecast month at lead time $\tau = 1080$ days for Icepack, Icepack-NN and Icepack-wclim predictions, at the six locations simulated.

smooth, incremental adaptation (such as online learning) provide little advantage. The ML model’s ability to generalize across such changes is loosely related to how strongly the underlying dynamical system responds to parameter modifications (Carrassi et al., 2008): in general, one might expect some degree of generalization as long as the system does not cross a bifurcation (also referred to as a tipping point in non-autonomous systems (Ghil and Sciamarella, 2023)), that would induce qualitatively different behavior from the version used in training. Here, we focus on transfer learning as a means to adapt a pretrained NN to a forecast model with a new set of (yet incorrect) calibrated parameters, and we assess under which conditions this adaptation provides better performance than retraining a model from scratch. Transfer learning has been studied recently as a tool to update the weights of a variational autoencoder in the context of a non-autonomous system (Pasmans et al., 2025).

5.2 Methodology and results

We adopt a fine-tuning transfer learning strategy (Iman et al., 2023), whereby NNs pretrained on a given *source* model are further trained on as little as possible data from a different *target* model, while retaining the original network architecture and using a reduced learning rate to preserve previously learned features. Their performance is then compared to NNs trained from scratch with progressively larger training sets. The same datasets previously described (Section 4.1) are used, focusing on ice volume error correction. All models are retrained over progressively longer training sets: the last two years are reserved for validation and testing, while earlier years are incrementally added to the training set (up to eight years in total), as illustrated in Table 3. Fine-tuning follows the same procedure, except training is initialized from pretrained models. Importantly, when transferring a pretrained

Number of training years	1994	1995	1996	1997	1998	1999	2000	2001	2002	2003
1										
2										
:										
8										

Table 3: Time-based dataset split used in the transfer learning experiments, illustrating the progressive enlargement of the training set. ■ Training set, ■ Validation set, ■ Test set

NN to a different task (i.e., the task of correcting model error of an incorrect physical model the NN has not seen in its training), the input and output normalization parameters (means and standard deviations) computed for pretraining, must be preserved to ensure consistency. Pretrained source models are those previously trained on the full eight-year training set (Section 4.2). For each training dataset size, both retraining and fine-tuning are evaluated using different learning rates, as shown in Figure S7. The comparison is then based on the best-performing learning rate (minimum validation loss) for each case.

Results for two source-target configuration pairs are shown in Figure 12. The two selected pairs ($m_09 \rightarrow m_24$ and $m_09 \rightarrow m_22$) illustrate a scenario where a poorly calibrated model with large errors (m_09) is refined to achieve configurations that are either more (m_24) or less (m_22) similar to the initial configuration within the parameter space (cf. Section S1). In both cases, the performance of fine-tuning and retraining tends to converge as the number of training years increases; however, fine-tuning delivers a clear advantage when a limited amount of training data is available (Figure 12a), which may translate into significant computational savings by reducing the need for extensive retraining. This advantage is not guaranteed (Figure 12b), as the effectiveness of fine-tuning appears to depend on the similarity between the source and target tasks.

Although the advantage of fine-tuning cannot be quantified strictly *a priori*, in this section, we propose a criterion to estimate its potential before performing additional training. To this end, a normalized MSE is introduced, $nMSE_{dir}$, defined as follows,

$$nMSE_{dir} = \frac{\left(\mathbf{g}(\hat{\theta}_{src}, \mathbf{z}_{trg}) - \mathbf{e}_{trg} \right)^2}{(\mathbf{e}_{trg})^2}, \quad (11)$$

where $\mathbf{g}(\hat{\theta}_{src}, \mathbf{z}_{trg})$ denotes the prediction by the NN pretrained on the source task with weights $\hat{\theta}_{src}$, evaluated on inputs \mathbf{z}_{trg} from the target task. The term \mathbf{e}_{trg} represents the corresponding forecast error of the target model configuration. Unlike the NN loss function, this metric is computed in physical space, enabling a fair comparison between training strategies. The metric $nMSE_{dir}$, where “dir” stands for *direct transfer*, measures the MSE obtained by directly applying the pretrained NN normalized by the uncorrected forecast MSE. Although a distance in parameter space may seem a natural way to quantify similarity between tasks in this context, we do not regard it

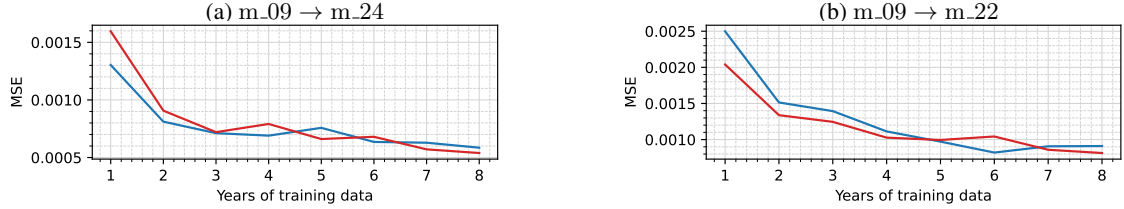


Figure 12: Validation MSE obtained with fine tuning (—) and retraining (—) as a function of the number of training years. The pretrained NN is trained on configuration m_09 and fine-tuned for configurations m_24 (a) and m_22 (b).

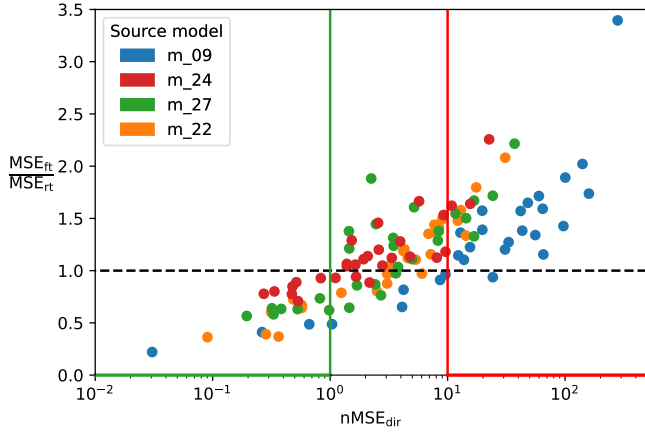


Figure 13: Scatter plot of the ratio between fine-tuning and retraining MSE, MSE_{ft}/MSE_{rt} , on the validation set, plotted against the metric $nMSE_{dir}$ (Eq.11). Both fine-tuning and retraining are performed using one year of training data. Each point refers to a single source-target configuration pair. Vertical green and red lines indicate mark $nMSE$ thresholds below (above) which fine-tuning is expected to perform better (worse) than retraining from scratch.

as reliable, as prior parameter distributions are often unavailable and the mapping from parameter variations to dynamical response is non-linear. To assess the relevance of the ratio defined in Eq. (11) as a criterion for estimating fine-tuning potential, we analyze multiple source-target configuration pairs: four pretrained source configurations, each targeting all remaining configurations. Fine-tuning and retraining are both performed using only one year of new training data. The results are summarized in Figure 13, which presents scatter plots of the ratio between fine-tuning and retraining MSE, MSE_{ft}/MSE_{rt} , computed on validation sets, plotted against $nMSE_{dir}$. As expected, for $nMSE_{dir}$ smaller than one, fine-tuning outperforms retraining ($MSE_{ft}/MSE_{rt} < 1$). This behavior is natural, since $nMSE_{dir} < 1$ indicates that the pretrained model already provides a better-than-baseline prediction, implying a meaningful alignment between source and target dynamics. In such cases, fine-tuning benefits from a favorable initialization that already captures relevant structure, whereas retraining must learn this structure from scratch with limited data. On the other hand, when $nMSE_{dir}$ exceeds ten, fine-tuning performs worse than retraining. For intermediate values between one and ten, outcomes are mixed, and no reliably predictive rule emerges, although a slight dependence on the pretrained source model is noticeable. To quantify how consistently the validation and test outcomes align within each $nMSE_{dir}$ region ($[0,1]$, $[1,10]$, $(10, \infty)$), we computed an agreement score, defined as the fraction of instances in which both sets indicate the same preference (fine-tuning or retraining). The resulting agreements for the three regions were 1.00, 0.70, and 0.97, respectively, with the reduced agreement in the intermediate range reflecting the increased ambiguity when performance ratios lie close to one. Overall, $nMSE_{dir}$ offers a simple, though possibly conservative, criterion to assess the potential benefit of fine-tuning before additional training, since the point at which fine-tuning ceases to be advantageous can shift to higher values depending on the pretrained source model.

6 Feature importance and physical interpretation

We complete the study by performing a feature importance analysis to identify the most effective predictor features. This may guide and lead to the identification of a minimal model depending on the degree of desired accuracy. Minimal models are not only computationally lighter but generally more interpretable. The analysis employs a Permutation-Importance-based Recursive Feature Elimination (PI-RFE) algorithm, which combines Recursive Feature Elimination (RFE) with Permutation feature Importance (PI, Breiman (2001)). At each iteration, the network is trained and the importance of each feature is estimated by randomly permuting its values in the validation set and measuring the corresponding drop in predictive performance. The least important feature is eliminated and the process is repeated until only one feature is left. Figure S6 illustrates the recursive feature elimination process for data relative to a specific model configuration. Recursive feature elimination establishes a feature-importance ranking, with features eliminated last occupying higher positions. Monitoring the validation loss during feature elimination can also help identify a reduced subset of relevant predictors. However, the order in which features are eliminated and the corresponding increase in validation loss varies across networks trained on different model configurations. By applying PI-RFE to each configuration and then aggregating the results, we can identify consistent patterns in feature importance and validation-loss behavior across all configurations. Specifically, we compute a feature-importance-rank frequency map (Figure 14), which shows, for each feature, the frequencies of its rankings across all models. The normalized frequency of feature X having rank k across models is defined as

$$\hat{f}_k(X) = \frac{1}{M} \sum_{m=1}^M \mathbf{1}_{\{R_m(X)=k\}}, \quad (12)$$

where M is the number of perturbed model configurations, m indexes the models, and $R_m(X)$ denotes the rank assigned to feature X by PI-RFE for model m . Features are grouped into five clusters of similar importance using agglomerative clustering based on the Wasserstein distance, implemented using utilities from SciPy (Virtanen et al., 2020) and scikit-learn (Pedregosa et al., 2011). These clusters are highlighted in Figure 14 through the color of the feature labels, with each cluster's mean rank reported in the legend. The least important cluster (C0) includes only precipitation rates (rain and snow), while the next cluster (C1) groups variables related to atmospheric forcing: air temperature, longwave radiation, and absorbed shortwave radiation. Since atmospheric forcing features are instantaneous snapshots, their high variability, and the additional intermittency of precipitation in particular, can plausibly explain their low rank. At the opposite end of the spectrum, the most relevant features for ice-volume error prediction (cluster C4) are ice concentration and ice volume forecasts, in agreement with previous findings on online error correction (Finn et al., 2023; Gregory et al., 2023). Interestingly, snow volume does not belong to this top-importance cluster, even though the model error in our experiments is rooted in the snow-physics parameterizations. Instead, together with a subset of ice-layer enthalpies, it forms cluster C3, within which the surface and bottom-layer enthalpies emerge as the most influential features. By integrating rapid surface-process variability, ice enthalpies retain long-term information that remains relevant at the 60-day forecast horizon. The remaining variables form a medium-importance cluster (C2), which includes the ice-layer enthalpies not assigned to C3, the outgoing longwave radiation, and the ice surface temperature.

The impact of feature elimination on the predictive performance of the NNs is assessed by examining how validation loss varies with a decreasing number of features during PI-RFE across all models. As shown in Figure 6, validation loss values obtained with the full feature set differ across models. To extract an averaged trend of validation loss as a function of feature count, each curve is normalized by the corresponding validation loss \mathcal{L}_0 computed with the full feature set: Figure 15 reports the individual model curves (colored by colormap) and the ensemble average (green). Validation loss begins to increase consistently after the removal of 6–7 features, which in most cases contain the atmospheric forcing variables (Figure 14), thereby confirming their negligible impact on predictive performance. The sharpest increase occurs when reducing from three to two features, indicating that acceptable performance requires, in addition to ice volume and concentration, at least one ice-layer enthalpy (most likely the surface layer). Finally, ML models with inherently poor performance (high \mathcal{L}_0) appear largely insensitive to feature elimination. In these cases, as discussed in Section 4.2, our NN corrections have trouble estimating the very small errors of the original uncorrected models, regardless of the number of features. Overall, these results suggest that a minimal feature set capable of matching the performance obtained with all variables would include the features in clusters C3 and C4 and possibly the two remaining enthalpies from C2 for physical consistency, yielding a total of ten feature variables. While alternative experimental setups employing longer or shorter time windows may alter the relative importance of intermittent versus long-memory variables, and thus which ice layers are most important in terms of their enthalpy, the aggregating effect of ice enthalpy is expected to persist across setups, granting it greater predictive power than atmospheric variables.

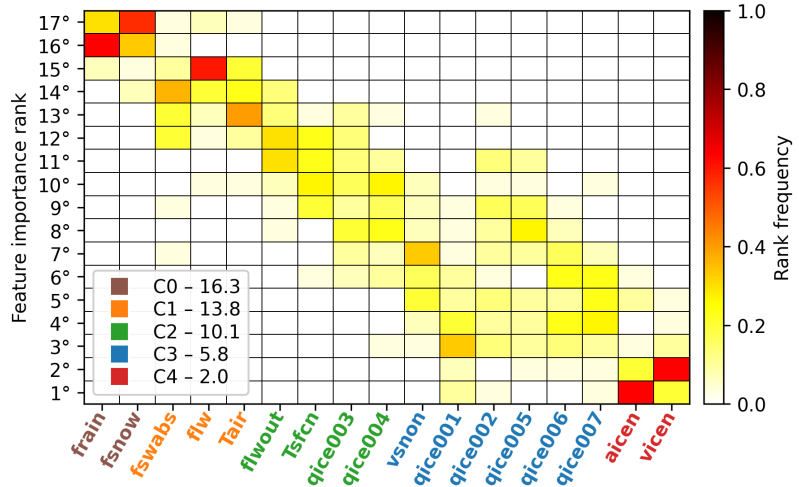


Figure 14: Feature-importance rank frequency map. Each column shows the frequency distribution of importance ranks over all the model configurations for the feature indicated on the x-axis (cf. Eq. (12)). Feature labels are colored according to their cluster of similarly important features, and the corresponding mean ranks are reported in the legend.

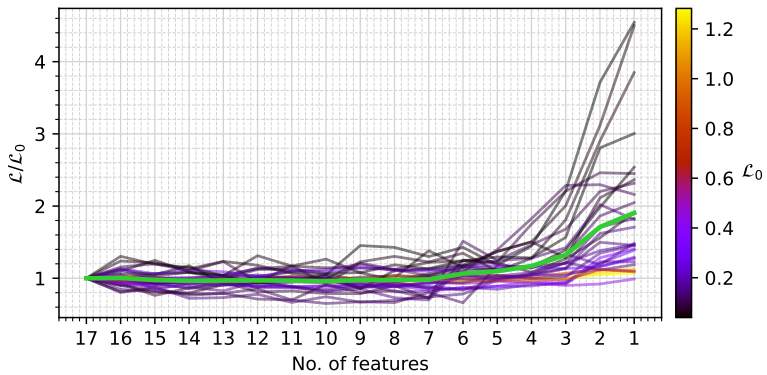


Figure 15: Normalized validation loss $\mathcal{L}/\mathcal{L}_0$ against number of features. Colormap lines refer to individual models, with color indicating loss obtained using the full feature set. The green line denotes the ensemble average.

7 Conclusions

We investigated the use of ML to estimate and correct model error arising from parameter misspecification in the state-of-the-art sea-ice column physical model Icepack. Experiments were conducted in an idealized setup, where true trajectories were generated using a reference Icepack configuration, while forecasts came from perturbed configurations with modified snow thermodynamics and radiative properties. For each perturbed configuration, NNs were trained to predict 60-day forecast errors in ice volume and concentration across different spatial locations. Our approach followed the hybrid-modeling strategy introduced in Brajard et al. (2021) and Farchi et al. (2021b). A key distinction from these earlier works is that, while they focused on chaotic autonomous systems, the model considered here (Icepack) is a forced, non-autonomous system, similar to those examined in Finn et al. (2023) and Gregory et al. (2023). Moreover, to isolate the impact of parametric error from DA and initial condition errors and to enable the characterization of error statistics within the perturbed parameters subspace, we intentionally assumed perfect and complete observations. This allowed us to bypass DA and train NNs directly on exact forecast errors rather than analysis increments. The physical model and NN corrections were integrated into hybrid frameworks (Icepack-NN), applying NN-based error corrections iteratively in a manner analogous to sequential DA. Ad-hoc post-processing ensured physical consistency, model restartability and numerical stability. Hybrid models were tested for forecasts up to 1080 days and compared with a climatology-based benchmark (Icepack-wclim). These experiments showed that NN corrections are most effective for models exhibiting substantial deviations from the truth, without degrading the performance of nearly perfect models. Hybrid simulations remained stable and robust to atmospheric-forcing and initial-condition errors, despite their absence during training. Across all configurations, NNs consistently outperformed the climatology-based approach, with Icepack-NN achieving nearly a 60% reduction in ice-volume RMSE, compared with less than 40% for Icepack-wclim.

Although the setup is idealized, our focus on errors connected to snow thermodynamics highlights that sufficiently long lead times are required for these errors to emerge and become detectable by ML methods. In operational systems, however, the training lead time is not a free parameter but is dictated by the DA cycle, which typically ranges from 5 to 7 days in sea-ice applications (Sakov et al., 2012; Zhang et al., 2021; Cipollone et al., 2023). As a result, DA-based ML bias-correction approaches applied to realistic sea-ice models are expected to primarily capture fast-growing errors associated with horizontal dynamics, whereas slower thermodynamic error components may require additional calibration or ad-hoc strategies to be effectively addressed.

Transfer learning experiments were conducted to assess how effectively a NN trained to correct one physical model configuration can be adapted to another. In the present study, configuration-specific training was adopted because the statistics of analysis increments depend on the underlying forecast model. Generally, a single NN trained across different forecast models represents an unavoidable compromise and should not be expected to be optimal for any individual model; likewise, a NN trained to correct a given model or configuration is not expected to generalize reliably to other contexts. This model dependence suggests that NNs typically need to be updated when the physical model is modified and, more broadly, whenever changes introduced in the DA system may alter the statistics of analysis increments. Updating NNs becomes particularly difficult when new observational products are introduced, since past reanalysis data, required for training a new NN and producing an updated hybrid model, cannot be reconstructed. We relied on fine-tuning of pretrained networks, whose performance is compared with networks retrained from scratch. For small dataset sizes, fine-tuning can be advantageous, though its effectiveness depends on the similarity between source and target tasks. Task similarity is not uniquely defined and cannot be inferred *a priori* from parameter differences, because even small parameter changes may trigger bifurcations and substantially alter error statistics. For this reason, a criterion was sought to estimate fine-tuning potential benefit, before actual training, using only one year of new training data. In particular, we considered the ratio between the pretrained network's MSE on the target task and the forecast MSE of the target model. Results showed that if the ratio is below one, fine-tuning is preferable, whereas if it is larger than 10, fine-tuning performs worse than retraining. For intermediate values, results are mixed; therefore, testing the two approaches is necessary. While this transferability metric is case-specific, its first threshold is expected to hold more generally: if the direct application of a pretrained model retains any meaningful skill, even marginal, this suggests some degree of alignment between source and target tasks and makes fine-tuning a reasonable choice. Notably, when applicable, fine-tuning can help mitigate overfitting on limited datasets and improve generalization to unseen data. Overall, these findings represent a first step toward developing practical guidelines and a systematic approach for the efficient and rapid adaptation of pretrained NNs through transfer learning, particularly in data-limited operational settings.

Finally, we carried out a feature importance analysis to assess the relative impact of input features on NN error prediction. Using permutation feature importance, a feature-importance-rank frequency map is derived. Atmospheric-forcing variables showed negligible importance, which is likely due to the high variability of the instantaneous snapshots used as inputs, particularly for precipitation, rather than to a lack of influence of the

forcing on error growth. Their impact might increase if integrated over the forecast window or in settings where forcing biases play a more prominent role. Conversely, ice concentration and volume emerged as the most influential features, as also reported in earlier studies (Finn et al., 2023). Moreover, the importance of enthalpy variables highlighted the relevance of thermodynamic state information for ML-based bias correction, particularly in regimes where forecast errors are dominated by thermodynamic processes. Their relevance in more realistic configurations, where errors are dominated by horizontal dynamics, remains to be assessed.

Future work will extend this framework to more realistic applications, incorporating horizontal sea-ice dynamics and relaxing the perfect-DA assumption. We will address challenges associated with the assimilation of satellite-derived sea-ice thickness, and further explore the generalization of atmospheric-forcing inputs from reanalyses to forecasts, which can exhibit systematic and lead-time-dependent differences. Another aspect worth exploring concerns the behavior of hybrid models in fully coupled ocean–sea-ice systems; as noted by Gregory et al. (2026), correcting only one component can expose the NN to out-of-sample inputs during free forecasts, since reanalysis constrains both components during training. Understanding and mitigating such mismatches will be essential for operational deployment.

ACKNOWLEDGEMENTS

GD and AC were supported by the MELTED project (*Machine Learning for Arctic ice prediction project*), funded by the Italian Ministry of University and Research (MUR) through the 2022 PRIN (Progetti di Rilevante Interesse Nazionale) call, including contributions from the National Recovery and Resilience Plan (NRRP). GD and AC also acknowledge support from the Scale-Aware Sea Ice Project (SASIP) funded by Schmidt Sciences, a philanthropic initiative that seeks to improve societal outcomes through the development of emerging science and technologies. Cerea is a member of Institut Pierre-Simon Laplace (IPSL).

DATA AVAILABILITY STATEMENT

The data that support the findings of this study are available from the corresponding author upon reasonable request.

CONFLICT OF INTEREST STATEMENT

The authors have no conflict of interest to declare.

References

Kaifeng Bi, Lingxi Xie, Hengheng Zhang, Xin Chen, Xiaotao Gu, and Qi Tian. Accurate medium-range global weather forecasting with 3d neural networks. *Nature*, 619(7970):533–538, 2023.

Marc Bocquet. Surrogate modeling for the climate sciences dynamics with machine learning and data assimilation. *Frontiers in Applied Mathematics and Statistics*, 9:1133226, 2023.

Marc Bocquet, Julien Brajard, Alberto Carrassi, and Laurent Bertino. Bayesian inference of chaotic dynamics by merging data assimilation, machine learning and expectation-maximization. *Foundations of Data Science*, 2 (1):55–80, 2020. doi: 10.3934/fods.2020004.

Cristian Bodnar, Wessel P Bruinsma, Ana Lucic, Megan Stanley, Anna Allen, Johannes Brandstetter, Patrick Garvan, Maik Riechert, Jonathan A Weyn, Haiyu Dong, et al. A foundation model for the earth system. *Nature*, pages 1–8, 2025.

Thomas Bolton and Laure Zanna. Applications of deep learning to ocean data inference and subgrid parameterization. *Journal of Advances in Modeling Earth Systems*, 11:376–399, 1 2019. ISSN 19422466. doi: 10.1029/2018MS001472.

Massimo Bonavita. On some limitations of current machine learning weather prediction models. *Geophysical Research Letters*, 51, 6 2024. ISSN 19448007. doi: 10.1029/2023GL107377.

Julien Brajard, Alberto Carrassi, Marc Bocquet, and Laurent Bertino. Combining data assimilation and machine learning to infer unresolved scale parametrization. *Philosophical Transactions of the Royal Society A*, 379 (2194):20200086, 2021.

Leo Breiman. Random forests. *Machine learning*, 45(1):5–32, 2001.

A. Carrassi, S. Vannitsem, and C. Nicolis. Model error and sequential data assimilation: A deterministic formulation. *Quarterly Journal of the Royal Meteorological Society*, 134(634):1297–1313, July 2008. ISSN 0035-9009,

1477-870X. doi: 10.1002/qj.284. URL <https://rmets.onlinelibrary.wiley.com/doi/10.1002/qj.284>.

Alberto Carrassi and Stéphane Vannitsem. Treatment of the error due to unresolved scales in sequential data assimilation. *International Journal of Bifurcation and Chaos*, 21(12):3619–3626, 2011.

Alberto Carrassi, Marc Bocquet, Laurent Bertino, and Geir Evensen. Data assimilation in the geosciences: An overview of methods, issues, and perspectives. *Wiley Interdisciplinary Reviews: Climate Change*, 9:1–79, 2018. ISSN 17577799. doi: 10.1002/wcc.535.

William E Chapman and Judith Berner. Improving climate bias and variability via cnn-based state-dependent model-error corrections. *Geophysical Research Letters*, 52(6):e2024GL114106, 2025.

Kang Chen, Tao Han, Fenghua Ling, Junchao Gong, Lei Bai, Xinyu Wang, Jing-Jia Luo, Ben Fei, Wenlong Zhang, Xi Chen, et al. The operational medium-range deterministic weather forecasting can be extended beyond a 10-day lead time. *Communications Earth & Environment*, 6(1):518, 2025.

Sukun Cheng, Ali Aydoğdu, Pierre Rampal, Alberto Carrassi, and Laurent Bertino. Probabilistic forecasts of sea ice trajectories in the arctic: Impact of uncertainties in surface wind and ice cohesion. *Oceans*, 1:326–342, 2020. ISSN 26731924. doi: 10.3390/oceans1040022.

F Chevallier, F Chéry, NA Scott, and A Chédin. A neural network approach for a fast and accurate computation of a longwave radiative budget. *Journal of applied meteorology*, 37(11):1385–1397, 1998.

Andrea Cipollone, Deep Sankar Banerjee, Doroteaciro Iovino, Ali Aydogdu, and Simona Masina. Bivariate sea-ice assimilation for global-ocean analysis-reanalysis. *Ocean Science*, 19(5):1375–1392, September 2023. ISSN 18120792. doi: 10.5194/os-19-1375-2023. Publisher: Copernicus Publications.

Simon Driscoll, Alberto Carrassi, Julien Brajard, Laurent Bertino, Marc Bocquet, and Einar Örn Ólason. Parameter sensitivity analysis of a sea ice melt pond parametrisation and its emulation using neural networks. *Journal of Computational Science*, 79:102231, 2024.

Danni Du, Feiyu Lu, and Alistair Adcroft. Reducing model biases with machine learning corrections derived from ocean data assimilation increments. *Authorea Preprints*, 2025.

C. Durand, T. S. Finn, A. Farchi, M. Bocquet, J. Brajard, and L. Bertino. Four-dimensional variational data assimilation with a sea-ice thickness emulator. *The Cryosphere*, pages 5613–5637, 2025. doi: 10.5194/tc-19-5613-2025.

A. Farchi, M. Chrust, M. Bocquet, and M. Bonavita. Development of an offline and online hybrid model for the integrated forecasting system. *Q. J. R. Meteorol. Soc.*, 151:e4934, 2025. doi: 10.1002/qj.4934.

Alban Farchi, Marc Bocquet, Patrick Laloyaux, Massimo Bonavita, and Quentin Malartic. A comparison of combined data assimilation and machine learning methods for offline and online model error correction. *Journal of Computational Science*, 55:101468, 2021a. ISSN 18777503. doi: 10.1016/j.jocs.2021.101468. URL <https://doi.org/10.1016/j.jocs.2021.101468>.

Alban Farchi, Patrick Laloyaux, Massimo Bonavita, and Marc Bocquet. Using machine learning to correct model error in data assimilation and forecast applications. *Quarterly Journal of the Royal Meteorological Society*, 147:3067–3084, 2021b. ISSN 1477870X. doi: 10.1002/qj.4116.

Tobias Sebastian Finn, Charlotte Durand, Alban Farchi, Marc Bocquet, Yumeng Chen, Alberto Carrassi, and Véronique Dansereau. Deep learning subgrid-scale parametrisations for short-term forecasting of sea-ice dynamics with a maxwell elasto-brittle rheology. *Cryosphere*, 17:2965–2991, 2023. ISSN 19940424. doi: 10.5194/tc-17-2965-2023.

Tobias Sebastian Finn, Charlotte Durand, Alban Farchi, Marc Bocquet, Pierre Rampal, and Alberto Carrassi. Generative diffusion for regional surrogate models from sea-ice simulations. *Journal of Advances in Modeling Earth Systems*, 16(10):e2024MS004395, 2024.

M. Ghil and D. Sciamarella. Review article: Dynamical systems, algebraic topology and the climate sciences. *Nonlinear Processes in Geophysics*, 30(4):399–434, 2023. doi: 10.5194/npg-30-399-2023. URL <https://npg.copernicus.org/articles/30/399/2023/>.

William Gregory, Mitchell Bushuk, Alistair Adcroft, Yongfei Zhang, and Laure Zanna. Deep learning of systematic sea ice model errors from data assimilation increments. *Journal of Advances in Modeling Earth Systems*, 15, 2023. ISSN 19422466. doi: 10.1029/2023MS003757.

William Gregory, Mitchell Bushuk, Yongfei Zhang, Alistair Adcroft, and Laure Zanna. Machine learning for online sea ice bias correction within global ice-ocean simulations. *Geophysical Research Letters*, 51, 2024. ISSN 19448007. doi: 10.1029/2023GL106776.

William Gregory, Mitchell Bushuk, Yong-Fei Zhang, Alistair Adcroft, Laure Zanna, Colleen McHugh, and Li-wei Jia. Advancing global sea ice prediction capabilities using a fully coupled climate model with integrated machine learning. *Science Advances*, 12(1):eady8957, 2026. doi: 10.1126/sciadv.ady8957. URL <https://advances.sciencemag.org/12/1/eady8957>.

<https://www.science.org/doi/abs/10.1126/sciadv.ady8957>.

Zikang He, Yiguo Wang, Julien Brajard, Xidong Wang, and Zheqi Shen. Correcting errors in seasonal arctic sea ice prediction of earth system models with machine learning. *The Cryosphere*, 19:3279–3293, 8 2025. ISSN 1994-0424. doi: 10.5194/tc-19-3279-2025. URL <https://tc.copernicus.org/articles/19/3279/2025/>.

Hans Hersbach, Bill Bell, Paul Berrisford, Shoji Hihara, András Horányi, Joaquín Muñoz-Sabater, Julien Nicolas, Carole Peubey, Raluca Radu, Dinand Schepers, et al. The era5 global reanalysis. *Quarterly journal of the royal meteorological society*, 146(730):1999–2049, 2020.

Christopher Horvat and Lettie A. Roach. Wiff1.0: A hybrid machine-learning-based parameterization of wave-induced sea ice floe fracture. *Geoscientific Model Development*, 15:803–814, 1 2022. ISSN 19919603. doi: 10.5194/gmd-15-803-2022.

Elizabeth Hunke, Richard Allard, David A. Bailey, Philippe Blain, Anthony Craig, Frederic Dupont, Alice DuVivier, Robert Grumbine, David Hebert, Marika Holland, Nicole Jeffery, Jean-Francois Lemieux, Robert Osinski, Jacob Poulsen, Anton Steketee, Till Rasmussen, Mads Ribernaard, Lettie Roach, Andrew Roberts, Matthew Turner, Michael Winton, and Denise Worthen. Cice-consortium/cice: Cice version 6.5.1, May 2024. URL <https://doi.org/10.5281/zenodo.11223920>.

Elizabeth Hunke, Richard Allard, David A. Bailey, Philippe Blain, David Clemens-Sewall, Anthony Craig, Frederic Dupont, Alice DuVivier, Robert Grumbine, David Hebert, Marika Holland, Nicole Jeffery, Jean-Francois Lemieux, Robert Osinski, Till Rasmussen, Mads Ribernaard, Lettie Roach, Andrew Roberts, Anton Steketee, Matthew Turner, Michael Winton, and Bin Zhao. Cice-consortium/icepack: Icepack 1.5.1, July 2025. URL <https://doi.org/10.5281/zenodo.16422921>.

Elizabeth C Hunke, David A Hebert, and Olivier Lecomte. Level-ice melt ponds in the los alamos sea ice model, cice. *Ocean Modelling*, 71:26–42, 2013.

Mohammadreza Iman, Hamid Reza Arabnia, and Khaled Rasheed. A review of deep transfer learning and recent advancements. *Technologies*, 11(2):40, 2023.

Diederik P. Kingma and Jimmy Ba. Adam: A method for stochastic optimization, 2017. URL <https://arxiv.org/abs/1412.6980>.

Alex Krizhevsky, Ilya Sutskever, and Geoffrey E Hinton. Imagenet classification with deep convolutional neural networks. *Advances in neural information processing systems*, 25, 2012.

Remi Lam, Alvaro Sanchez-Gonzalez, Matthew Willson, Peter Wirsberger, Meire Fortunato, Ferran Alet, Suman Ravuri, Timo Ewalds, Zach Eaton-Rosen, Weihua Hu, et al. Learning skillful medium-range global weather forecasting. *Science*, 382(6677):1416–1421, 2023.

Liam Li, Kevin Jamieson, Afshin Rostamizadeh, Ekaterina Gonina, Moritz Hardt, Benjamin Recht, and Ameet Talwalkar. A system for massively parallel hyperparameter tuning, 2020. URL <https://arxiv.org/abs/1810.05934>.

William H Lipscomb. Remapping the thickness distribution in sea ice models. *Journal of Geophysical research*, 106:13989–14000, 2001. doi: <https://doi.org/10.1029/2000JC000518>. URL <https://agupubs.onlinelibrary.wiley.com/doi/abs/10.1029/2000JC000518>.

PA O’Gorman and JG Dwyer. Using machine learning to parameterize 1012 moist convection: Potential for modeling of climate, climate change, and 1013 extreme events. *Journal of Advances in Modeling Earth Systems*, 10(10):1014, 2018.

Ivo Pasmans, Yumeng Chen, Tobias Sebastian Finn, Marc Bocquet, and Alberto Carrassi. Ensemble kalman filter in latent space using a variational autoencoder pair. *arXiv preprint arXiv:2502.12987*, 2025.

Jaideep Pathak, Shashank Subramanian, Peter Harrington, Sanjeev Raja, Ashesh Chattopadhyay, Morteza Mardani, Thorsten Kurth, David Hall, Zongyi Li, Kamyar Azizzadenesheli, et al. Fourcastnet: A global data-driven high-resolution weather model using adaptive fourier neural operators. *arXiv preprint arXiv:2202.11214*, 2022.

F. Pedregosa, G. Varoquaux, A. Gramfort, V. Michel, B. Thirion, O. Grisel, M. Blondel, P. Prettenhofer, R. Weiss, V. Dubourg, J. Vanderplas, A. Passos, D. Cournapeau, M. Brucher, M. Perrot, and E. Duchesnay. Scikit-learn: Machine learning in Python. *Journal of Machine Learning Research*, 12:2825–2830, 2011.

Stephan Rasp, Michael S Pritchard, and Pierre Gentine. Deep learning to represent subgrid processes in climate models. *Proceedings of the national academy of sciences*, 115(39):9684–9689, 2018.

Stephan Rasp, Stephan Hoyer, Alexander Merose, Ian Langmore, Peter Battaglia, Tyler Russell, Alvaro Sanchez-Gonzalez, Vivian Yang, Rob Carver, Shreya Agrawal, et al. Weatherbench 2: A benchmark for the next generation of data-driven global weather models. *Journal of Advances in Modeling Earth Systems*, 16(6):e2023MS004019, 2024.

Pavel Sakov, F Counillon, L Bertino, KA Lisæter, PR Oke, and A Koralev. Topaz4: an ocean-sea ice data assimilation system for the north atlantic and arctic. *Ocean Science*, 8(4):633–656, 2012.

Alan S Thorndike, Drew A Rothrock, Gary A Maykut, and Roger Colony. The thickness distribution of sea ice. *Journal of Geophysical Research*, 80(33):4501–4513, 1975.

Adrian K Turner, Elizabeth C Hunke, and Cecilia M Bitz. Two modes of sea-ice gravity drainage: A parameterization for large-scale modeling. *Journal of Geophysical Research: Oceans*, 118(5):2279–2294, 2013.

Jorge R Urrego-Blanco, Nathan M Urban, Elizabeth C Hunke, Adrian K Turner, and Nicole Jeffery. Uncertainty quantification and global sensitivity analysis of the los alamos sea ice model. *Journal of Geophysical Research: Oceans*, 121(4):2709–2732, 2016.

Pauli Virtanen, Ralf Gommers, Travis E. Oliphant, Matt Haberland, Tyler Reddy, David Cournapeau, Evgeni Burovski, Pearu Peterson, Warren Weckesser, Jonathan Bright, Stéfan J. van der Walt, Matthew Brett, Joshua Wilson, K. Jarrod Millman, Nikolay Mayorov, Andrew R. J. Nelson, Eric Jones, Robert Kern, Eric Larson, C J Carey, İlhan Polat, Yu Feng, Eric W. Moore, Jake VanderPlas, Denis Laxalde, Josef Perktold, Robert Cimrman, Ian Henriksen, E. A. Quintero, Charles R. Harris, Anne M. Archibald, Antônio H. Ribeiro, Fabian Pedregosa, Paul van Mulbregt, and SciPy 1.0 Contributors. SciPy 1.0: Fundamental Algorithms for Scientific Computing in Python. *Nature Methods*, 17:261–272, 2020. doi: 10.1038/s41592-019-0686-2.

Peter A.G. Watson. Applying machine learning to improve simulations of a chaotic dynamical system using empirical error correction. *Journal of Advances in Modeling Earth Systems*, 11:1402–1417, 5 2019. ISSN 19422466. doi: 10.1029/2018MS001597.

Oliver Watt-Meyer, Noah D. Brenowitz, Spencer K. Clark, Brian Henn, Anna Kwa, Jeremy McGibbon, W. Andre Perkins, and Christopher S. Bretherton. Correcting weather and climate models by machine learning nudged historical simulations. *Geophysical Research Letters*, 48, 8 2021. ISSN 19448007. doi: 10.1029/2021GL092555.

Yong-Fei Zhang, Mitchell Bushuk, Michael Winton, Bill Hurlin, Xiaosong Yang, Tom Delworth, and Liwei Jia. Assimilation of satellite-retrieved sea ice concentration and prospects for september predictions of arctic sea ice. *Journal of Climate*, 34(6):2107–2126, 2021.

Supporting Information

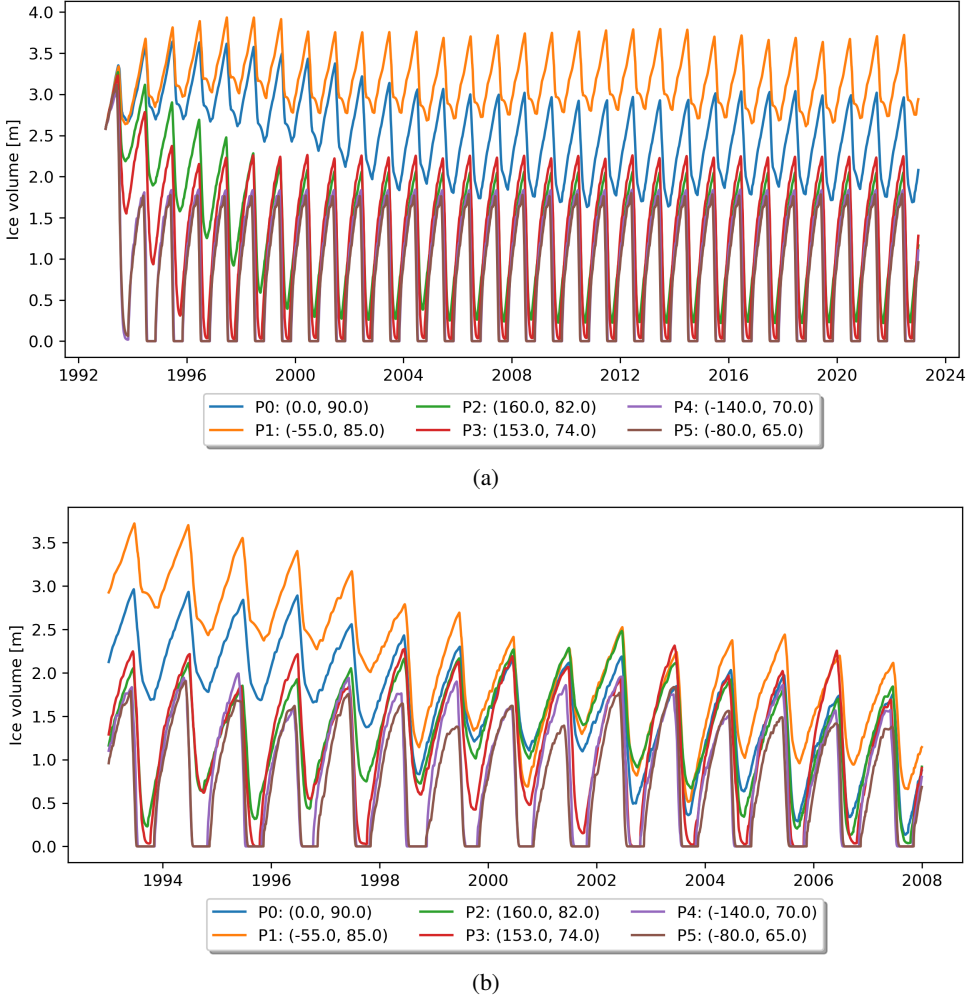


Figure S1: (a) Sea ice volume time series at the six selected locations, obtained from the ‘truth’ reference model forced cyclically with atmospheric conditions from 1993. (b) Same as (a), but with simulations initialized from the final yearly cycle of (a) and driven by time-varying atmospheric forcings.

S1 Parametric error metrics

Perturbed configurations are characterized by the Mahalanobis distance from the reference configuration and between each other. Such distance d between two generic configurations $\mathbf{c}_i, \mathbf{c}_j$, is defined as follows:

$$d(\mathbf{c}_i, \mathbf{c}_j) = \|(\mathbf{c}_i - \mathbf{c}_j)\|_P \quad (\text{S1a})$$

where $\mathbf{c}_i = (p_{1i}, p_{2i}, \dots, p_{Ni})$ corresponds to a point in an N -dimensional parameter subspace, representing the i -th parameters’ configuration and $P = S^{-1}$ the precision matrix. Moreover, to evaluate the similarity between configurations, it is useful to evaluate the angle cosine $\cos(\theta)$ between configuration position vectors in the metric space defined by the Mahalanobis distance, whose origin is represented by the reference configuration, as shown in Equation (S2b).

$$\mathbf{e}_k = \mathbf{c}_k - \mathbf{c}_0 \quad (\text{S2a})$$

$$\cos(\theta)_{i,j} = \frac{\langle \mathbf{e}_i, \mathbf{e}_j \rangle_P}{\|\mathbf{e}_i\|_P \|\mathbf{e}_j\|_P}. \quad (\text{S2b})$$

The metrics defined in Equations (S1a) and (S2b) are computed for each member relative to the reference configuration, as well as to any other member. The results, depicted in Figure S2 offer an overview of parameters’ perturbations magnitude and similarities for the configurations generated.

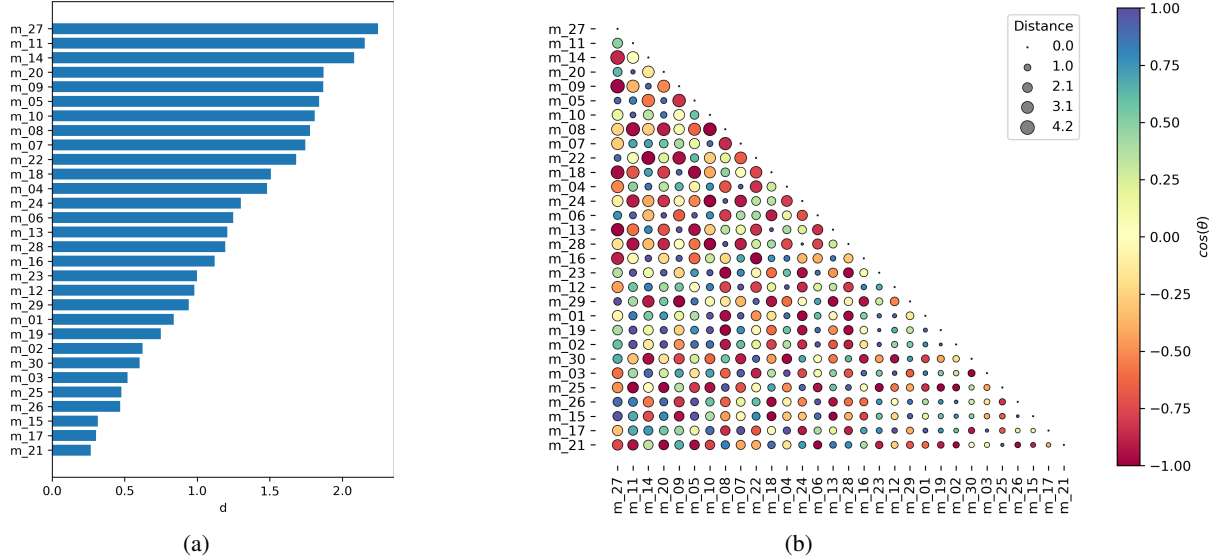


Figure S2: PC2: (a) Distances computed according to Eq. (S1a) between each member in PC2 and reference configuration. (b) Marker size represent the distance between configuration pairs, whereas coloring represents the cosine of the angle between configuration vector pairs according to Eq. (S2b)

S2 Dependence of Icepack forecast errors on lead time and start date

As detailed in Section 3.1, the uncorrected Icepack model is initialized from the true reference states at 522 start dates across six locations, and subsequently integrated for 180 days. The dependence of the prediction errors on the lead time and start date is investigated in Fig. S3. It displays the RMSE^{ens}, averaged over start dates within each calendar month, separately for each of the six locations. It is evident that the error shows little dependence on the start date. Nevertheless, a pronounced diagonal band of near-zero error appears, particularly in the panels along the right column, corresponding to lower-latitude locations P3, P4 and P5. This behavior of the error reflects the complete melt of sea ice during summer, when the error approaches zero, followed by the subsequent refreezing during which the misspecification of the snow physics parametrization progressively manifest and lead to the error growth.

Based on the result in Fig. S3, we choose to design our ML-based bias correction to act at the lead time of 60 days (cf. Section 3.1). This choice ensures a sufficient signal-to-noise ratio and allows systematic errors to emerge, while avoiding excessive skill degradation between successive corrections.

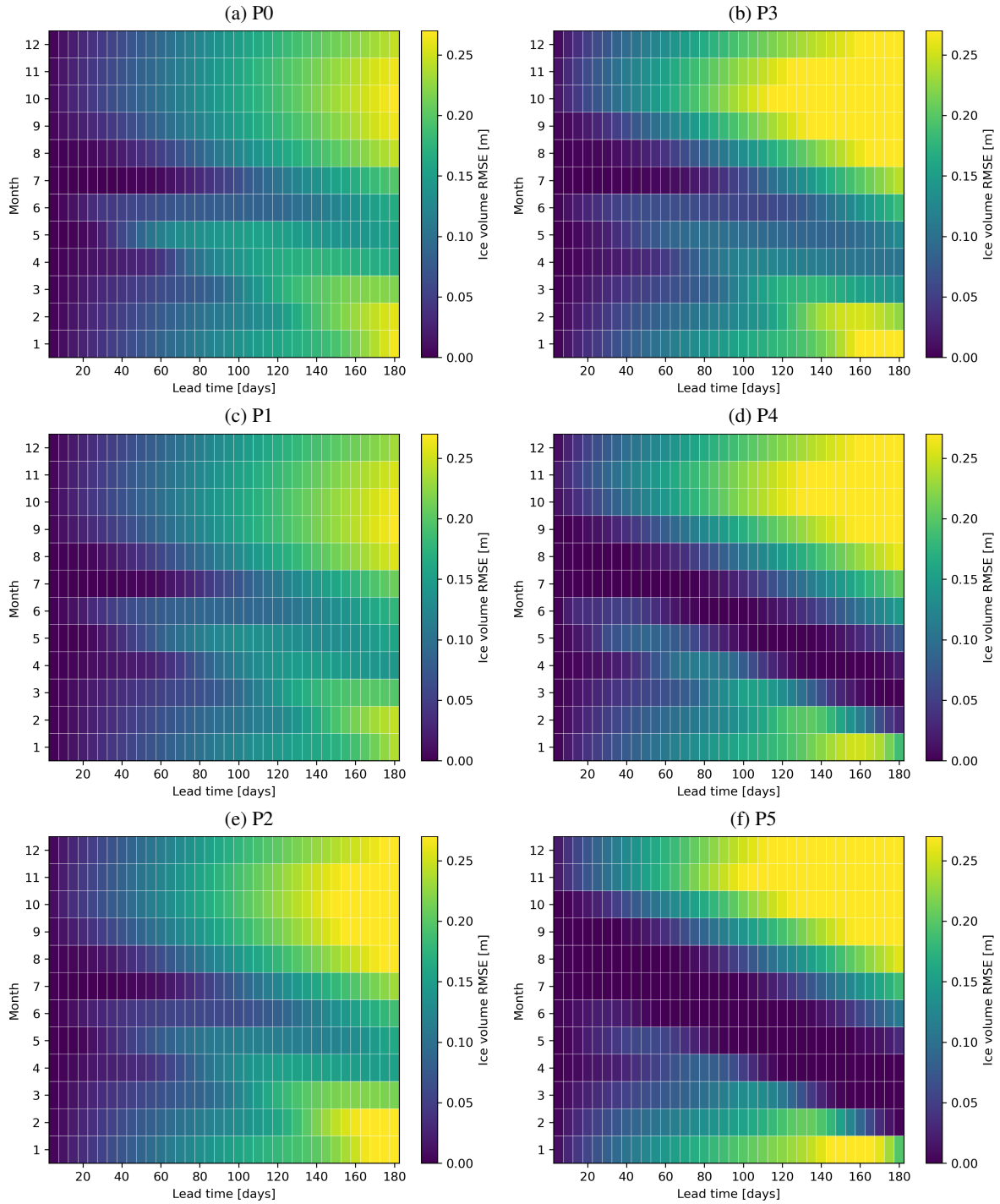


Figure S3: RMSE^{ens} of the uncorrected Icepack forecasts, as function of lead time and starting month, at the six locations under study.

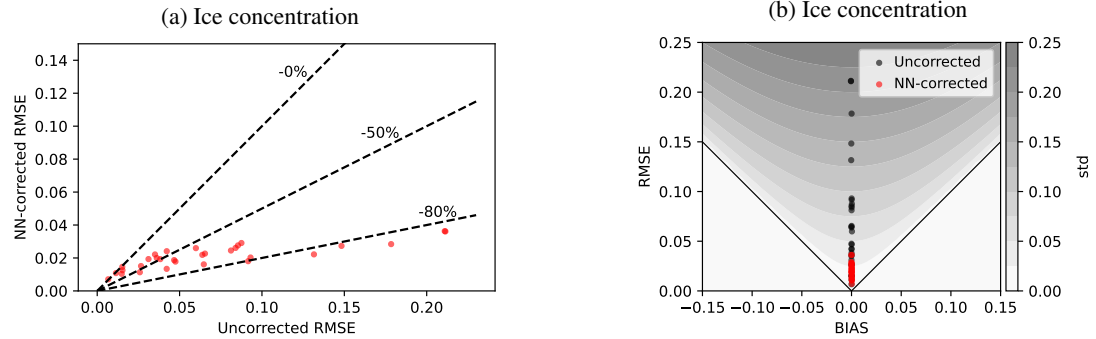


Figure S4: Left panels (a) shows scatter plot of the residual RMSE after NN correction versus the uncorrected Icepack RMSE for ice concentration on the test dataset. Dashed lines indicate three levels of RMSE reduction, as labeled in the figure. Right panel (b) displays scatter plots of BIAS and RMSE before and after correction for ice concentration, with shaded contours representing the corresponding standard deviation.

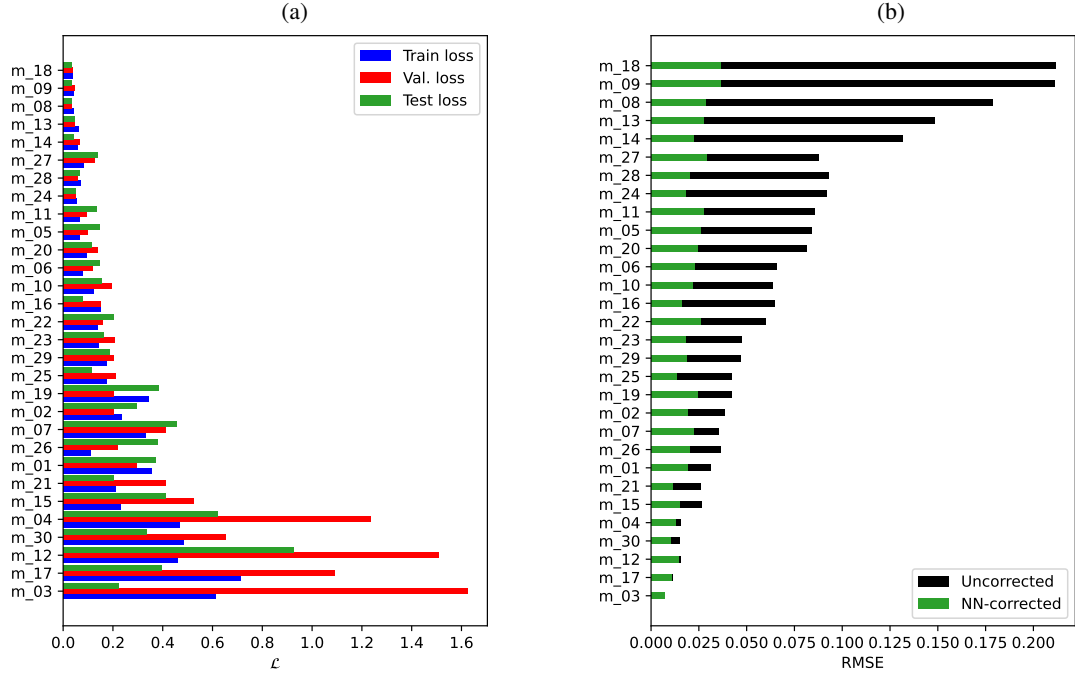


Figure S5: (a) Loss function \mathcal{L} relative to ice concentration errors prediction, computed over training, validation and test datasets using the best-performing neural network for each ensemble member. (b) RMSE of ice concentration forecasts and the residual value after correction by the NN. Ensemble members are sorted as in Figure 5(b).

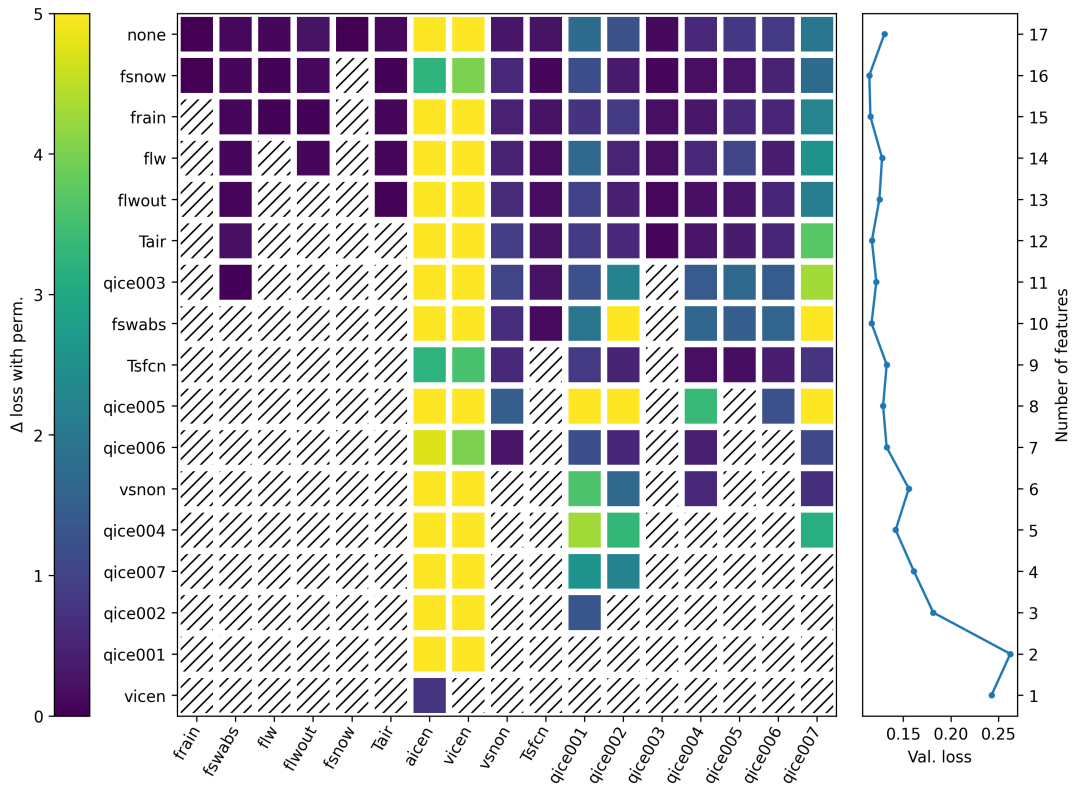


Figure S6: Recursive feature elimination for a single ensemble member. Rows represent successive iterations (top to bottom). Square colors denote the increase in validation loss caused by permuting each feature, relative to the reference obtained without permutations. Reference validation loss values are shown in the right panel. At each iteration, the feature whose permutation produces the smallest increase is removed, indicated by hatching in the subsequent row and labeled on the left.

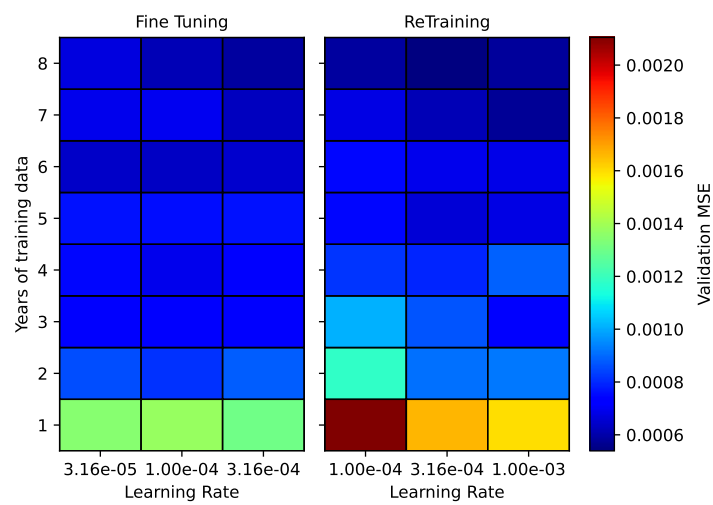


Figure S7: Validation MSE comparison between Fine-Tuning and Re-Training strategies for predicting ice volume forecast error of model m_24, across different learning rates and numbers of training years. In the fine-tuning experiments, the neural network was pretrained on data from model configuration m_09.